Draft version April 3, 2009
Preprint typeset using LaTeX style emulateapj v. 10/09/06

arXiv:0904.0657v1 [astro-ph.GA] 3 Apr 2009

STELLAR METALLICITIES AND KINEMATICS IN A GAS-RICH DWARF GALAXY: FIRST CALCIUM TRIPLET SPECTROSCOPY OF RGB STARS IN WLM

Ryan Leaman[1], Andrew A. Cole[2], Kim A. Venn[1], Eline Tolstoy[3], Mike J. Irwin[4],
Thomas Szeifert[5], Evan D. Skillman[6], Alan W. McConnachie[1,7]
[1]University of Victoria, Canada, [2]University of Tasmania, Australia, [3]Kapteyn Institute, The Netherlands, [4]Institute of Astronomy, U.K., [5]ESO-Chile, Chile, [6]University of Minnesota, U.S., [7]National Research Council of Canada, Herzberg Institute of Astrophysics, Canada

Draft version April 3, 2009

ABSTRACT

We present the first determination of the radial velocities and metallicities of 78 red giant stars in the isolated dwarf irregular galaxy WLM. Observations of the calcium II triplet in these stars were made with FORS2 at the VLT-UT2 in two separated fields of view in WLM, and the [Fe/H] values were conformed to the Carretta & Gratton (1997) ($[\mathrm{Fe/H}]_{CG97}$) metallicity scale. The mean metallicity is $\langle[\mathrm{Fe/H}]\rangle = -1.27 \pm 0.04$ dex, with a standard deviation of $\sigma = 0.37$. We find that the stars in the inner field are more metal rich by $\Delta[\mathrm{Fe/H}] = 0.30 \pm 0.06$ dex. These results are in agreement with previous photometric studies that found a radial population gradient, as well as the expectation of higher metallicities in the central star forming regions. Age estimates using Victoria-Regina stellar models show that the youngest stars in the sample (< 6 Gyr) are more metal rich by $\Delta[\mathrm{Fe/H}] = 0.32 \pm 0.08$ dex. These stars also show a lower velocity dispersion at all elliptical radii compared to the metal-poor stars. Kinematics for the whole red giant sample suggest a velocity gradient approximately half that of the gas rotation curve, with the stellar component occupying a thicker disk decoupled from the HI rotation plane. Taken together, the kinematics, metallicities, and ages in our sample suggest a young metal-rich, and kinematically cold stellar population in the central gas-rich regions of WLM, surrounded by a separate dynamically hot halo of older, metal poor stars.

Subject headings: galaxies: abundances — galaxies: evolution — galaxies: dwarf — galaxies: individual (WLM) — galaxies: kinematics and dynamics

1. INTRODUCTION

Dwarf galaxies play a critical role in our understanding of the assembly of galaxies in LCDM cosmologies. With masses of 10^8 to 10^9 $M_\odot$, these galaxies are thought to be similar to the proto-galactic fragments that merged and collapsed to form large galaxies (e.g., Navarro et al. 1997; Moore et al. 1999; Madau et al. 2001). Analysing the survival of these low mass objects, particularly through reionisation (Ricotti & Gnedin 2005; Gnedin & Kravtsov 2006), is crucial to constraining galaxy formation models. For example, what was the minimum halo mass that could retain its baryons through reionisation? Theoretical constraints on low mass galaxies are also provided by examining the detailed characteristics of the various types of dwarf galaxies (irregulars, spheroidals, and the new ultra faint dwarfs) and the connections between them. Are dwarf irregular galaxies simply dSph which have undergone recent gas mergers (Demers et al. 2006; Brook et al. 2007)? Are transition galaxies gas-rich dwarf galaxies being subject to ram pressure stripping (e.g., Pegasus dwarf galaxy; McConnachie et al. 2007)? Are signatures of thick stellar disks or spheroidal components expected in dwarf irregular galaxies? How will the dynamics of the stellar populations compare to the gas motions in the low mass galaxies? This line of research can be carried out on the nearby Local Group galaxies, thus defining near-field cosmology.

Dwarf irregular (dIrr) galaxies hold a special status in the analysis of the Local Group galaxies because most are relatively isolated. Detailed studies of the nearby dwarf spheroidal galaxies have revealed complex and varied star formation histories that have left behind distinct stellar populations (Tolstoy et al. 2004; Battaglia et al. 2006; Bosler et al. 2007). However, interpretation of the kinematics of these stellar populations, and therefore evolution of the nearby dSph galaxies, is complicated by the fact that they exist in the dark matter halos of the MW and M31 (i.e., their stellar populations have likely been tidally stirred). On the contrary, dwarf irregular galaxies are relatively *isolated* low mass galaxies. Evolved stellar populations in dIrrs may prove to be excellent tracers of the dynamical history of low mass dwarf galaxies at early times, and therefore excellent comparisons for galaxy formation models.

However, there have been few studies of the kinematics of the stellar populations in isolated dIrrs and no detailed spectroscopic analysis of their *older* stellar populations due to their distances.[1] This is significant because various galaxy formation scenarios predict different characteristics for the stellar populations in early dwarf galaxies; e.g., simulations by Mayer et al. (2006) predict disk like systems that become more spheroidal through tidal interactions and ram pressure stripping, whereas Kaufmann et al. (2007) suggest that dwarf galaxies start

Electronic address: rleaman@uvic.ca

---

[1] We note that Tolstoy et al. (2001) examined the calcium II triplet feature in 23 RGB stars in the closest dIrr, NGC 6822 ($V_{TRGB} \sim 21$), and found most stars were young and metal-rich, representative of the dominant young population at the brightest magnitudes.

out as thick, puffy systems and through gas losses and tidal interactions become more disk like.

In this paper, we present the first spectroscopic analysis of the calcium II triplet (CaT) feature in a sample of RGB stars in the dIrr galaxy WLM. WLM is a typical low-luminosity, high gas fraction late-type dwarf irregular galaxy. A summary of its fundamental parameters is listed in Table 1. The nearest neighbour to WLM is the Cetus dSph, which lies 200 kpc away (Whiting et al. 1999). WLM's distance to the Milky Way is estimated at $\sim 932 \pm 33$ kpc (McConnachie et al. 2005), and its separation from M31 is ∼820 kpc, therefore this is one of the most isolated galaxies in the Local Group. WLM has a heliocentric velocity of -130 km s^{-1} (Jackson et al. 2004) and a modest velocity with respect to the Local Group barycentre, -29 km s^{-1}, implying that it may have recently passed apocentre and is turning around. Additionally, WLM lies out of the Galactic plane, which minimizes foreground contamination and reddening.

High dispersion spectra have been taken for a few bright A and B-type supergiant stars in WLM (Venn et al. 2003; Bresolin et al. 2006; Urbaneja et al. 2008). Detailed analyses of these stars provide the present day metallicities and abundance ratios ([Fe/H]$= -0.38 \pm 0.2$, Venn et al. 2003; [O/H]~ -0.85, Bresolin et al. 2006; [Z]$= -0.87 \pm 0.06$, Urbaneja et al. 2008), but offer little information on the intermediate or old age populations. The older red giant branch stars in these isolated dIrrs are too faint for high dispersion spectroscopic analyses, even with 8m class telescopes. Studies of HII regions from emission line spectroscopy yield [O/H] $= -0.83$ (Skillman et al. 1989; Hodge & Miller 1995; Lee et al. 2005), but provide no information about the chemistry of the gas in the early stages of the galaxy. Interestingly, WLM has revealed minor discrepancies in chemistry between the young stars and H II regions - possibly due to inhomogeneous mixing (e.g., Venn et al. 2003 found [O/H] $= -0.21$ in one A supergiant; Lee et al. 2005 find [O/H] $= -0.83 \pm 0.06$ from emission line measurements in two HII regions, which included the [OIII] λ 4363 line). Neutral gas studies in WLM have been used to map the HI envelope extent and small scale spatial and velocity structures (Huchtmeier et al. 1981; Barnes & de Blok 2004; Jackson et al. 2004; Kepley et al. 2007).

The old population in WLM was first sampled by Hodge et al. (1999) who derived a metallicity from isochrone fitting to deep HST imaging of the lone globular cluster, WLM-1. HST photometry and wide field INT imaging (Minniti & Zijlstra 1997; Rejkuba et al. 2000; McConnachie et al. 2005) also identified young and old stellar populations in the form of an extended blue main sequence, and a horizontal branch on the CMD. These photometric surveys were also used to find the distance and reddening to WLM, and to estimate the range in metallicity on the RGB. Photometric analyses of C and M stars in WLM by Battinelli & Demers (2004) have argued against the presence of an old extended halo in WLM, opposite to the conclusion from Minniti & Zijlstra (1997) based on the interpretation of their CMDs. However, differential reddening within WLM may be affecting all of these photometric analyses; the recent Spitzer IRAC survey of AGB stars in WLM (Jackson et al. 2007) has shown the patchy presence of dust throughout WLM.

The use of the empirically calibrated near infrared calcium triplet lines provides a new method for studying the stellar population in WLM. Situated at λ ∼8498, 8542, 8662 Å, they are optimally located with minimal contamination from other spectral features and near the peak in flux for these evolved red stars. The summed equivalent widths (EWs) of these lines are well calibrated to allow a representative placement of a star onto a given [Fe/H][2] scale, and sensitive enough from medium resolution spectra to perform well out to large distances in the local volume. The metallicity index is also well correlated with the iron abundances ([Fe/H]) determined by Carretta & Gratton (1997) from high dispersion spectroscopy of Galactic globular clusters. This scale shows a linear correlation with the CaT W' index, unlike the Zinn & West (Zinn & West 1984) scale based upon the Q_{39} spectrophotometric index. Previous large scale calibration studies (Rutledge et al. 1997; Cole et al. 2004; Carrera et al. 2007b; Battaglia et al. 2007) confirmed the robustness of the CaT method over a range of ages ($0.25 \leq$ Gyr ≤ 13) and over the metallicity range expected for the stars in a gas rich dIrr galaxy ($-2.5 \lesssim$ [Fe/H] $\lesssim +0.47$). A growing number of CaT studies have been carried out for several Local Group galaxies, including the Magellanic clouds (Pont et al. 2004; Cole et al. 2005; Grocholski et al. 2006; Carrera et al. 2007a) and dSph galaxies (Tolstoy et al. 2004; Battaglia et al. 2006; Koch et al. 2006; Bosler et al. 2007), which further tests the robustness of the CaT method in different environments.

In the following sections, we discuss the observations, the data reduction methods, and spectral analysis of CaT spectroscopy adopted in this paper. These sections are particularly important since this work represents a CaT analysis of some of the faintest RGB stars for which velocities *and* metallicities have been determined at moderate S/N. The main challenge has been to minimize the velocity and metallicity errors. Although the final uncertainties are slightly larger than CaT surveys of closer galaxies, we have been able to determine a new metallicity distribution function for WLM and characterize the spatial and velocity variations in its stellar populations for the first time.

2. OBSERVATIONS AND DATA REDUCTIONS

2.1. *Target Selection and Photometric Calibration*

Relatively isolated and bright stars near the tip of the RGB ($V_{mag} \sim 23$) were selected from 150 second V and I band preimaging exposures from FORS2 on the VLT (Appenzeller et al. 1998). The data were bias corrected and flatfielded in IRAF[3] and instrumental photometry was obtained using DAOPHOT/ALLFRAME (Stetson 1994). Stars were selected from the tip of the RGB (TRGB) to those within half a magnitude below the RGB tip (instrumental I band), and colors consistent with RGB membership. This meant that stars were selected to have instrumental colours spanning the apparent width of the RGB (i.e., constrained to a colour range of 1.1 magnitudes) to avoid heavy contamination by red supergiants and M stars. Our targets were selected to encompass a broad area of the galaxy's high density (gas and stellar) regions, as well as lower density outer areas.

---

[2] The notation [Fe/H] = $\log(\mathrm{Fe/H})_* - \log(\mathrm{Fe/H})_\odot$

[3] IRAF(Image Reduction and Analysis Facility) is distributed by the National Optical Astronomy Observatory, which is operated by the Association of Universities for Research in Astronomy, Inc., under cooperative agreement with the National Science Foundation

The FORS2 preimaging photometry was then matched to extant INT WFC V, i band photometry of a 0.25 square degree region centered on WLM (see McConnachie et al. (2005) for further details), due to the preimaging being taken under non-photometric conditions. This allowed us to use standard magnitudes and colours for our analysis. A list of INT WFC stars for matching was created based on colour, magnitude, and location, and these stars were further filtered based on sharpness and ellipse parameters. As the stars were uniformly selected to be bright and isolated, we acknowledge that a selection effect may appear in areas of low stellar density. However, this is unavoidable in resolved stellar spectroscopy at such large distances, and simply necessitates that care be taken in the interpretation of the results. Four globular clusters (47Tuc, NGC1851, NGC1904, M15) spanning a range of metallicities, were also chosen for calibration purposes, as described in §3.1.1.

2.2. *Data Acquisition and Reduction*

The observations for this study of WLM and the four calibrating clusters were taken during several nights at the VLT in late 2003 (see Table 1). The MXU (Mask eXchange Unit) mode was used with the FORS2 instrument at the Cassegrain unit of VLT's UT4 (Yepun) telescope, note this was before the instrument was relocated to UT1 (Antu) in 2004. The 83 RGB stellar targets ranged in magnitude from $22.1 \leq \mathrm{V}_{mag} \leq 24.0$, requiring exposure times on the order of 40 minutes for individual images even with an 8m class telescope. Slit acquisition images were taken for approximately 150 seconds in Bessell I band, to confirm the pointing and slit alignment prior to science exposures. The parameters for the object science exposures on the observational dates in question are shown in Table 2.

Figure 1 shows a representative view of the FORS2/MXU fields used in this study of WLM. For reference, the INT WFC fields are the four red rectangles. The FORS2 instrument was used with the MXU in order to provide selectable custom cut slit plates; a configuration which allowed the preselected RGB stars to be fit within $1'' \times 8''$ slits to minimize the required observation time spent for the program. A spectroscopic order separation filter (OG590+32) and the standard resolution collimator were used in conjunction with a volume phased holographic grism to obtain the stellar spectra for each slit target. The grism, designated GRIS_1028+29, provided wavelength coverage from roughly 7730Å to 9480Å with a central wavelength of λ_c = 8600Å, and a dispersion of 28.3Å/mm. FORS2 is equipped with a mosaic of two red-optimized 2k×4k MIT CCDs (15μm pixels) with very low fringe amplitude in the spectral range of the CaT lines. With 2×2 binning and 100khz readout characteristics, and the above mentioned optical path, the effective field of view across the instrument was $6.8' \times 5.7'$. The two component chips have a pixel scale of $0.252''$/pixel, where the pixel size is 0.86Å (2×2 binning). This setup produced observations with resolving power R $\sim$ 3400. The gain for both chips was 0.7 ADUs/e^-, with the readnoise being 2.7e^- and 3.15e^-, respectively. Each of the large blue boxes in Figure 1 is representative of the full two chip CCD field of view. The representative seeing conditions for the observations at VLT ranged from $0.61'' \leq$ FWHM $\leq 1.52''$ over the course of our science exposures.

Once obtained in service mode at the telescope, the data were reduced using a variety of standard IRAF tasks for bias, overscan and flatfield corrections to the two dimensional images. Typically each science image used a bias correction combined from 10 individual bias exposures, along with 5 individual screen flat field exposures for each of the chips, which were reduced independently. The objects were cleaned for cosmic rays using several iterations of the COSMICRAYS task. In order to minimize any error in the final aperture extraction or wavelength calibration, custom tasks were run to remove warping in the stellar trace and sky lines (particularly the far corners of the chips) due to light path distortions or chip alignment issues. A custom IRAF script was used to provide a preliminary correction to the drooping artifact of the stellar trace as a function of row position on the CCD. A second script was then used to linearize and orthogonalize the dispersion coordinate and spatial coordinate to optimize subtraction of the sky lines (see Grocholski et al. 2006). Following these corrections, aperture extraction was run on all science spectra, resulting in one dimensional spectral images for all the stars in the sample. We used a standard sky line atlas in conjunction with the IDENTIFY and REIDENTIFY tasks to provide dispersion solutions for the wavelength calibration of the spectra. Typical line fits involved $\sim$ 40 OH sky emission features taken from Osterbrock & Martel (1992). The typical accuracy of the wavelength solution is within $\sim$ 0.04Å based on the rms of the solutions. Finally, the task CONTINUUM removed the curvature of the spectrum and normalized the flux distribution to allow for the most accurate measurements of the regions of interest (the calcium triplet lines).

Prior to combination, we adjusted the wavelength zeropoint of each spectrum for the heliocentric correction. This was a non-trivial concern for the radial velocity measurements as our individual exposures were spread over several months (See Table 2). A date dependent shift was applied to each spectrum, such that their observed velocities were corrected back to a common epoch at the date of the first observation. This resulted in at most a $\sim$ 1.2Å correction to the spectra. The final spectra include the median of eight individual exposures for each of 79 RGB stars (four stars were thrown out due to spectral contamination or photometry matching issues). The typical signal to noise ratio for our combined images ranged between $16 \lesssim (\mathrm{S/N}) \lesssim 23$ per pixel (1 pixel = 0.86Å).

3. SPECTRAL ANALYSIS

3.1. *Equivalent Width Measurements*

The choice of techniques for equivalent width measurements had to be carefully considered, given the moderate signal to noise of our combined spectra ($\sim$ 20). As noted by Cole et al. (2004), the line wings are typically underestimated with a pure Gaussian profile fit, and are much more accurately modeled with the sum of a Gaussian and Lorentzian fit. However, for low signal-to-noise spectra, when the line FWHM are on the order of the spectral resolution, the contaminating noise features effectively nullify any difference between using a Gaussian, Lorentzian, or the sum of the two. Therefore an accurate characterization of the spectrographic setup is necessary in low resolution Calcium triplet spectroscopic studies. For this reason, the choice was made to use a simple pixel to pixel integration of the line profiles. Due to the low signal-to-noise of the spectra, the integration was taken over the range where the line wings intersected the global continuum level. The continuum normalized spectra had an average continuum at unity already, no adjustment was made to the flux zeropoint. The integration yields a wavelength, core density, and equivalent width for each line. Multiple independent measurements were made by remeasuring the same line repeatedly, with a systematic deviation in equivalent width of approximately 1%. Figure 2 shows a sample spectrum in the region of the Ca II triplet lines for one star in our sample.

As a consistency check, we performed simultaneous measurements on the reduced calibrating clusters (which had a much higher signal to noise) using both the pixel to pixel integration method and the profile fitting programs from Cole et al. (2004). The linear fit between the methods' measurements (see Figure 3) was used to develop a transformation function which put our equivalent widths onto the same scale as in Cole et al. (2004), thereby allowing us to adopt a variety of their calibrations as described in the next section.

3.1.1. *Placement onto the Metallicity Scale*

Armandroff & Da Costa (1991) first showed the usefulness of the CaT feature as a metallicity indicator in individual evolved giant branch stars. Using the summed equivalent widths of the CaT lines, as well as the star's V magnitude above the horizontal branch, a reduced equivalent width could be formulated. When observed for Galactic globular cluster stars, which also had high dispersion spectroscopic [Fe/H] estimates, this low resolution CaT estimator could be used to provide an empirical metallicity index. Several studies (e.g., Rutledge et al. 1997; Cole et al. 2004) have since explored these empirical calibrations over a large range of stellar ages and metallicities. Cole et al. (2004) found minimal deterioration in the CaT calibration over extremes in age and metallicity. This is particularly relevant for dwarf galaxy studies where we expect a mixed stellar population based on CMD analyses (e.g., Dolphin 2000). In this paper, we adopt the calibrations determined by Cole et al. (2004) based on many clusters which were made with the same instrument (FORS2) at the VLT, and adopted similar data reduction techniques as used here. The spread in cluster ages in the full sample studied by Cole et al. (2004) is ideal for analyzing a dIrr galaxy like WLM. Recently, Battaglia et al. (2007), Carrera et al. (2007a), and Battaglia et al. (2008) have confirmed the robustness of the CaT spectroscopic method as a means for metallicity estimates in dwarf galaxies. These studies specifically checked the appropriateness of the CaT index as a proxy for [Fe/H] in cases of varying [α/Fe], [Ca/Fe], and age. Additionally, studies by Rutledge et al. (1997) and Cenarro et al. (2001) showed that the CaT index transforms in a well understood way between different authors' studies.

To use any of the calibrations requires a summed equivalent width determination for each star. Each of the three calcium triplet line measurements were combined in an unweighted fashion to yield a summed equivalent width per star.

$$\Sigma W = W_{8498} + W_{8542} + W_{8662} \tag{1}$$

The justification to use all three lines will be discussed in §3.2.2 and §3.2.3 with respect to our errors. With this relation it is now possible to form the calcium index, W' defined as:

$$W' = \Sigma W + \beta(V - V_{HB}) \tag{2}$$

The term in the parentheses provides a correction for the changes in T$_{eff}$ and $log(g)$ for stars in different phases on the red giant branch. A cooler temperature and lower surface gravity play non-trivial roles in the formation of the CaT line profiles and the continuum in these evolutionary stages. Theoretical and empirical work (Jorgensen et al. 1992; Cenarro et al. 2002) has confirmed this complicated interplay of the calcium line strengths with stellar parameters such as temperature and gravity. Thus, this term is important in removing the gravity dependence of the lines with respect to the continuum in the CaT analysis. Our V magnitudes are taken from the INT WFC catalogue and associated database as mentioned in §2.1. We adopted the horizontal branch at $V_{HB} = 25.71 \pm 0.09$ mag (Rejkuba et al. 2000), and take $\beta = 0.73 \pm 0.04$Å mag^{-1} from Cole et al. (2004). Using the Carretta & Gratton (1997) scale, the calcium index is converted to a metallicity ([Fe/H]$_{CG97}$) as follows:

$$[Fe/H]_{CG97} = (0.362 \pm 0.014)W' - (2.966 \pm 0.032) \tag{3}$$

The zero point and slope were determined by Cole et al. (2004), and estimated as accurate to $\leq$ 4%. This means that the majority of our uncertainties are from other factors, which we will discuss below in the following section.

Figure 4 shows a plot of the summed calcium II equivalent widths (ΣW) against the V magnitude above the horizontal branch per star. The fiducial solid lines show the spacing in metallicity given by the calibration from Cole et al. (2004).

3.1.2. *Error Analysis*

To examine the various sources of uncertainty in our calculations, all errors from the equivalent width measurements to placement on the [Fe/H]$_{CG97}$ scale were recorded. As no standalone error estimate was provided by the pixel integration routine used in measuring a line equivalent width, W, we adopted the Cayrel formula (see Eq. 7; Cayrel 1988, also Battaglia et al. 2007) as:

$$\langle \Delta W_n^2 \rangle^{\frac{1}{2}} \simeq (1.6(FWHM_n \delta x)^{\frac{1}{2}}\epsilon) + (0.10W_n) \tag{4}$$

where the pixel size is $\delta x = 0.86$Å, and the average rms continuum accuracy is $\epsilon \sim \frac{1}{(S/N)_{avg}}$. As the pixel integration measurements did not contain information on the FWHM of the line, that value was determined as follows. A test set of Gaussian and Lorentzian fits were made to the strongest line (8542 Å) in 18 stars, using the line profile fitting routine SPLOT. A Gaussian-Lorentzian blended estimate of the FWHM was estimated from an arithmetic average of the two fit values. These were then plotted as a function of measured equivalent width (from the pixel integration method). A linear regression was fit; an estimate of the FWHM to be used in this formula for the rest of the stars was then determined based on their equivalent width values. The FWHM values for the sub-sample of stars used in this step showed a standard deviation of $\sigma_{fwhm} = 1.06$Å.

With a full set of equivalent widths and representative FWHM values, Equation 4 could be used to find a realistic uncertainty in a given line. These steps were repeated for all three CaT lines, then added in quadrature for the error in the summed equivalent width, ΣW. An additional term was added to this in quadrature, to account for the variation in equivalent width measuring methods used. This term was determined from the rms dispersion about the best fit in the transformation to the Cole et al. (2004) equivalent width measurement system (see §3.1.1)

The final expression for the uncertainty in metallicity is now formulated into one equation, allowing for simple partial derivative based error propagation. Defining an equation for metallicity based on the following equation of observables or calibrated variables:

$$f = [Fe/H]_{CG97} = c_1 \left[\Sigma W + \beta(V_{HB} - V)\right] - c_2 \qquad (5)$$

allowed us to express the total uncertainty as:

$$\Delta[Fe/H]^2 = \left\{ \left(\frac{\partial f}{\partial c_1}\right)^2 (\Delta c_1)^2 + \left(\frac{\partial f}{\partial \Sigma W}\right)^2 (\Delta \Sigma W)^2 + \left(\frac{\partial f}{\partial \beta}\right)^2 (\Delta\beta)^2 + \ldots \right\} \qquad (6)$$

The simple mathematical propagation is reasonable and justified, as the the variables involved in Equation (6) are uncorrelated and independent. This propagation and error accounting results in an average uncertainty in metallicity of Δ[Fe/H] = ±0.25 dex.

3.1.3. *Three Line Justification*

We performed a parallel reduction omitting the weakest line in the calcium series (8498 Å). The purpose of this exercise was to test whether the uncertainties in constructing the calcium index, W', were significantly reduced with the rejection of the lowest signal source. Composite two-line indices were created in order to compare the relative errors that occurred for exclusion of each line in the creation of the calcium index. The *average* relative error for the full 80 star sample on any of the line pairs, $\frac{\Delta W_{nm}}{W_{nm}}$ where n and m are the first, second or third lines of the Ca II triplet, were calculated to be $\frac{\Delta W_{23}}{W_{23}} = 0.10$, $\frac{\Delta W_{13}}{W_{13}} = 0.12$, and $\frac{\Delta W_{12}}{W_{12}} = 0.11$ for the pairs. This minimal deviation, suggests that inclusion of all three lines is warranted, because the equivalent width measures do not dominate the random error budget, and thus there is no benefit to dropping the 8498 Å line.

3.2. *Radial Velocity Measurements*

Radial velocities were measured from the strong calcium lines which had previously had a wavelength dispersion solution applied from the sky OH lines. The low signal to noise of the individual frames necessitated that we perform the cross correlation radial velocity calculations on the combined spectra, rather than each individual image. As such, heliocentric velocity corrections were tailored to the individual exposures and applied prior to combining the spectra, due to the long temporal baseline (roughly four months) of the observations. Once shifted and combined, the spectra were ready for radial velocity computation with the aid of template stars and a Fourier cross correlation routine (FXCOR). A total of 23 template radial velocity stars, observed with the same instrument setup, were used with the cross correlation routine. This computation provided error analysis automatically, with the median error in the heliocentric velocities being $\langle \delta V_{hel} \rangle = \pm 6$ km s^{-1}. Systematic velocity errors due to a star's position in the slit were removed by centroiding the stars relative to the slit centre. The fact that this procedure was done on combined spectra resulted in small absolute corrections, as the $\sqrt{n}$ statistics meant that the individual slit errors were minimized in the combination and correction steps. The typical shift for the slit error on an individual exposure is approximately 6-9 km s^{-1}, and we note that this shift produces negligible uncertainties in the equivalent width error. The final average absolute corrections to the slit centering errors on the combined spectra were on the order of ≤ 1.5 km s^{-1}.

Our sample of RGB stars has a mean velocity of $\langle V_{hel} \rangle = -130 \pm 1$ km s^{-1}, identical to the heliocentric velocity for WLM derived from neutral HI studies Jackson et al. (2004); Kepley et al. (2007). Only one foreground star was found, with radial velocity $V_{hel} = +48$ km s^{-1}, leaving us with 78 stars total. Given the location of WLM with respect to the Galactic plane and the colour and magnitude cuts in our preselection routine, it is not surprising that there were so few foreground objects.

3.3. *Age Derivations*

An estimate of the relative ages of our sample of RGB stars was determined using the Victoria-Regina stellar evolution tracks (VandenBerg et al. 2006). Given the extended SFH of WLM (Mateo 1998; Dolphin 2000) and the gas rich nature of dIrr galaxies, we expect a significant range in red giant ages in the dataset.

A CMD of the target stars in two metallicity bins, along with the fiducial sequences for M68 and 47Tuc, is shown in Figure 5. As the stars were selected across a wide range in (V-I) colours, the spectroscopic CaT [Fe/H] estimates allow us to break the age-metallicity degeneracy and provide a more complete understanding of the evolved populations in WLM. The age derivation procedure and error estimates of the relative stellar ages are more fully described by Leaman (2008)[4], however a brief outline is given below.

---

[4] This thesis work is freely available for download at:

To determine an age from the Victoria-Regina models, a value of $[Fe/H]_{CaT}$, V, and (V-I) is required for each star, as well as global values for distance and reddening to WLM (see Table 1) and an assumption about the α-element enhancement level. The $[\alpha/Fe]$ value to use for the WLM sample is not clear especially given the age and metallicity range of the evolved populations here (e.g., dSph stars show $[\alpha/Fe] = +0.3$ for metal-poor stars, but show subsolar ratios for increasing metallicity, Tolstoy et al. 2003; Venn & Hill 2008). $[\alpha/Fe] = +0.3$ was adopted based on the results from galactic globular clusters which were used to calibrate the CaT method here; however the effect of computing the ages with $[\alpha/Fe] = 0.0$ was found to be minor. Systematic effects (e.g., an evolutionary model's treatment of mixing length, convective overshooting, CNO abundances, radiative diffusion, gravitational settling etc.) between the models and observations were removed by comparing the isochrones to homogeneous globular cluster photometry from the CADC website[5]. The location of each star in the dereddened plane was used to interpolate a best age estimate amongst tracks of the appropriate metallicity for that star.

RGB stars can only evolve to luminosities approaching the tip of the RGB when the core becomes significantly electron-degenerate before the onset of core helium burning. Thus there is a lower limit to the age of the first-ascent RGB stars that could possibly be included in our sample, typically around 1.6 Gyr. At a given metallicity, this age marks the blue edge of the colour distribution of RGB stars. In cases where the star was bluer than allowed by this condition, an arbitrary age marker of 1 Gyr was assigned as an aid to interpreting the sample properties. Similarly, those redward of the oldest available track (18 Gyr) were assigned an age of 18 Gyr and a significant error (discussed below). As seen in Table 3, roughly one third of the stars are below the 1.6 Gyr cutoff, and most of those are found in the bar field of WLM.

Formal errors on the ages were adopted by folding in the uncertainty in the spectroscopic metallicities, as well as the uncertainties in the photometry. While other astrophysical factors could impact the positions of the stars on the CMD (e.g., variations in relative internal reddening), we are unable to explicitly quantify these effects. Figure 13 of Cole et al. (2005) illustrates the effect that some of these factors can have on the ages. Given those dependencies and the value of a typical metallicity error of ± 0.25 dex, the random error in age is $\sim \pm 50\%$.

The technique used here for deriving ages can be applied successfully in globular cluster populations in the MW (Tolstoy 2003). However studies using identical methods in dwarf galaxies have found it much more difficult to assign ages to evolved stars. Tolstoy et al. (2003) first showed that the evolved stars in dSph galaxies often lay blueward or redward of the full age parameter space (see the discussion in §3.2 Tolstoy et al. 2003; also Tolstoy 2003). This phenomenon has also been seen in the LMC (Cole et al. 2005). This wide range of colours is clear in our Figure 5, where we overlay GGC fiducial sequences (M68; [Fe/H]$\sim$-2.0, and 47 Tuc [Fe/H]$\sim$-0.7) onto a metallicity binned colour magnitude diagram of WLM. Notable are both metal poor and metal rich WLM stars[6] blueward of the fiducial sequence for M68. The majority of these stars are more metal rich than M68, suggesting that we are seeing a range of ages in our sample younger than typical globular cluster ages. In Figure 5 we also point out one star (STARID 19203), at $(V-I)_0 \sim 2.5$, and note that a greater uncertainty should be applied to this star's parameters as it may be subject to excessive reddening, or spectral contamination (notably, from weak TiO bands).

The question that we are left with is whether the bluest stars in our age derivations (those with inferred ages $\leq$1.6 Gyr), are really intermediate-mass stars on the early-asymptotic giant branch or are true low-mass stars on the first-ascent RGB, influenced by uncertainties in composition or differential reddening. If the majority of the bluest stars *are* truly 1 Gyr or less, then it is reasonable to look for concentrations of their more-evolved descendants (e.g., thermally-pulsing AGB stars). Among Local Group dwarfs, WLM has been found to have an extraordinarily large ratio of carbon- to M-stars, $C/M = 12.4 \pm 3.7$ (Battinelli & Demers 2004). This large population of carbon stars, along with the high recent star formation of WLM, does suggest that the majority of stars in our youngest age bin are truly young. Note that these young stars are not likely to be differentially reddened AGB or RSG contaminants, as cross-correlation with UKIRT WFCAM *JHK* photometry rules this out. However, early-AGB stars ascending from the horizontal branch towards the thermally-pulsing (carbon star) phase can occupy the same CMD space as a bona fide RGB star, and this becomes quite likely in a composite population such as WLM's. We note that if an RGB star is in fact an early AGB star, at a given metallicity the age of that star would be $\sim 30\%$ older than we infer here (for further discussion see Cole et al. 2005).

4. ANALYSIS AND DISCUSSION OF WLM

In this paper, we have determined the [Fe/H] and radial velocity values for 78 *individual* RGB stars in WLM. These can be used to examine the structure, kinematics, and chemical evolution history of this galaxy for the first time in conjunction with derived age estimates. This is unique, as all previous studies of supergiant stars (Venn et al. 2004; Bresolin et al. 2006; Urbaneja et al. 2008) and HII regions (Skillman et al. 1989; Hodge & Miller 1995; Lee et al. 2005) sampled the young population and offer little insight into the earlier epochs of formation and evolution of this galaxy. Similarly, photometric studies (Minniti & Zijlstra 1997; Hodge et al. 1999; McConnachie et al. 2005) were only able to provide global views of the metal poor population, and were subject to degeneracies in age and metallicity.

To begin our analysis, elliptical radii were determined for all of the stars in our sample. The position angle of WLM was taken to be 181° (Jackson et al. 2004) and the eccentricity 0.59 (Ables & Ables 1977). After transforming the equatorial coordinates into the transverse

---

[5] url: http://www3.cadc-ccda.hia-iha.nrc-cnrc.gc.ca/community/STETSON/standards/

[6] In this, and other representations throughout the paper, the metallicity split to characterize "metal rich" and "metal poor" RGB stars is made at $[Fe/H] = -1.27$ dex - approximately the median and mean value of our sample.

http://hdl.handle.net/1828/1325

ξ, η plane, and calculating the axial components of the ellipse for a given star, the elliptical radius (r_{ell}) was determined from the geometric mean of the semi-major and semi-minor axes. These elliptical radii have uncertainties due to the inclination with which WLM appears to observers (69°, which is not assumed in the calculations; Ables & Ables 1977). A given star may of course sit off the major plane of the galaxy - thus the calculated elliptical radii has an intrinsic degeneracy with the star's true distance from the plane of the disk.

A summary of the spatial and photometric properties for the 78 RGB stars in this sample are listed in Table 3. This includes the metallicity, age, radial velocity, and elliptical radii values as well.

4.1. *Chemistry*

The metallicity distribution function from our full sample of stars provides the first detailed insight into the chemistry of the evolved population of WLM. The top panel of Figure 6 shows the MDF for the WLM sample subdivided into the bar and north fields. The global mean (-1.28 ± 0.03, $1\sigma = 0.37$)[7] and peak (~ -1.30) values of the MDF are slightly higher than the photometric determinations, but consistent within errors. For example, Hodge et al. (1999) derived [Fe/H] = -1.51 ± 0.09 by isochrone fitting to the lone GC in WLM, McConnachie et al. (2005) found [Fe/H] $= -1.5 \pm 0.2$ (assuming no alpha-element enhancements) from empirically calibrated RGB colours, and Minniti & Zijlstra (1997) found [Fe/H] $= -1.45 \pm 0.2$, again from the photometric properties of the RGB. These photometric metallicity estimates essentially give lower limits, as younger stars will be shifted bluer on the RGB. Our higher results confirm that effect - as shown by our higher metallicities and range of ages for this composite population.

The MDF in Figure 6 shows a sharp drop off at the low end, with very few metal poor stars below [Fe/H] ≤ -1.8. Dolphin (2000) suggested that there was a significant star formation event 9-12 Gyr ago with an enrichment up to $[\mathrm{Fe/H}]_0 = -2.18 \pm 0.28$, however those stars do not appear in our sample. The low metallicity dropoff is primarily due to observational difficulties in attempting to sample a sizeable relative number of low [Fe/H] stars. Metal poor stars at this evolutionary locus are difficult to find in any galaxy due to a population bias resulting from mass dependent stellar evolutionary timescales (c.f. Cole et al. 2008). For a given time interval, more young, high mass, high metallicity stars will evolve to the TRGB than older, low mass, metal poor stars in the same time interval. The dominant fraction of young stars at the TRGB is large enough to outnumber the metal poor old stars, despite the contradictory initial relative numbers of the IMF. This effect will be enhanced in the presence of any age-metallicity relationship and is still present for populations with extended SFHs like WLM. In order to quantify the probability that the metallicities in our sample are drawn from a Gaussian parent distribution (which we don't expect due to the extended SFH, but wish to quantify), we performed a Kolmogorov-Smirnov (K-S) test on the cumulative metallicity distribution function (CMDF). The probability that the distribution was Gaussian is $\sim 8 \times 10^{-19}$. More interesting is a comparison to a metallicity distribution predicted by a simple closed or leaky box chemical evolution model. The bottom panel of Figure 6 shows our cumulative metallicity function compared to predicted distributions from leaky box models with a range of values for the parameter 'c', which controls the effective yield. The K-S probabilities that our distribution is drawn from one of the simple one zone models is $\leq 4\%$ for all models shown. Our distribution clearly shows a lower number of metal poor stars compared to these models.

Not surprisingly, the young stars that make up the metal rich half of our sample are found preferentially in the bar field of WLM (see Figure 6 top panel). Several tracers of high active SF are observed in this inner field, notably the strong and numerous HII regions (Hodge & Miller 1995; Youngblood & Hunter 1999) consistent again with the most enriched material being found at low r_{ell}.

This is more clearly visualized in the top panel of Figure 7, where the mean metallicity decreases by ∼0.3 dex with distance from the galactic core. From that figure we find a radial metallicity gradient of $\frac{\partial [Fe/H]}{\partial r} = -0.14 \pm 0.02$ dex/kpc. This smooth gradient may however be a line of sight superposition of two (or more) spatially localized subpopulations, mimicking a smooth radial profile.

This population change is consistent with the results from the photometric study by Minniti & Zijlstra (1997). The [Fe/H] values show a dispersion in metallicity that is roughly constant over the sampled region of the galaxy ($\sigma = 0.32$), similar to previous analyses. A two sided Kolmogorov-Smirnov test of the bar and north field cumulative metallicity distributions reveals that they have a very small probability of being drawn from the same parent distribution ($P = 0.005$). Splitting our sample into those stars with $r_{ell} \leq 0.1$ deg. and $r_{ell} > 0.1$ deg. and running the same K-S test, results in a similar probability ($P = 0.024$). This would appear to strengthen the interpretation of distinct spatial populations in WLM, as the inner and outer CMDFs show statistically different properties - not just different mean metallicities.

The bottom panel of Figure 7 shows the cumulative radial number density (CDF) of metal poor and metal rich stars as a function of elliptical radius from the center of WLM. The metal poor stars are found in more uniform numbers independent of radial position within the galaxy, whereas the more metal enhanced stars are found preferentially closer to the center of WLM.

In Figure 8, we compare the unbinned CMDFs for three age bins of our sample. In each bin, we have compared the WLM subsample to predicted CMDFs from a leaky, and closed box chemical evolution model. While our sample deviates from the simple models in the youngest age bins, the oldest age bin ($t > 6$ Gyr) shows a large probability of being drawn from a distribution approximated by the closed box model. We might naively expect that our oldest stars would have a characteristic shape to their metallicity distribution that would be more closely approximated by a closed box scenario, where little infall or outflow occurs. The deviations at younger ages presumably occur with the increase of accreted gas, and as such, the CMDF of our younger stars begins to vary from the shape predicted by a closed box model. However, there is an additional astrophysical effect that must be considered. As mentioned in paragraph two of this section, the evolutionary flux through the TRGB results in higher numbers of young stars in that locus than older, low mass, metal poor stars. This effect means that our 78 star sample is a slightly skewed example of the true [Fe/H] distribution at the TRGB. As such, one should keep in mind that the probabilities found in the K-S tests are really describing how our sample is comparing to the closed box models - presumably the true metallicity distribution of WLM would have more metal poor stars, and the K-S probabilities would be higher. This population bias is much more prominent in the youngest age bin, and at the older bin is less of a factor, and so these stars may result in a more representative sample of WLM's metallicity distribution. With larger numbers of stars it will be possible to quantify how much of the probability change with age is due to an evolutionary population bias, and how much may be attributed to infall of pristine gas.

---

[7] It should be noted our observed spread in metallicities should be compared to the intrinsic uncertainty in obtaining our individual [Fe/H] estimates (i.e., Δ[Fe/H]=$\pm$0.25 dex)

4.2. *Chemodynamics*

Figure 9 shows the results of our radial velocity analysis, presented as two velocity distribution functions (VDFs) for the bar and north field. Each field has been further subdivided into metal poor and metal rich subsamples. We note the peaked, Gaussian distributions around the mean values of $\langle v_{north} \rangle = -136 \pm 3$ km s^{-1} and $\langle v_{bar} \rangle = -126 \pm 3$ km s^{-1} for the north and bar field samples respectively. Comparing these subsamples shows that the *mean velocities* of the north and bar, metal poor and metal rich, populations are consistent (i.e., $\langle v_{NMP} \rangle = \langle v_{NMR} \rangle = -136 \pm 3$ km s^{-1}; $\langle v_{BMP} \rangle = \langle v_{BMR} \rangle = -126 \pm 4$ km s^{-1}). This indicates that the general bulk motion of both subgroups of stars in a given field holds in accordance with the group mean. However the *velocity dispersions* of the metallicity subpopulations, do not show the same uniform characteristics. The velocity dispersions of the metal poor subsamples for the north and bar fields are larger than the metal rich samples in both fields. We find: $\sigma_{v(NMP)} = 19$ km s^{-1}, $\sigma_{v(NMR)} = 12$ km s^{-1}, $\sigma_{v(BMP)} = 20$ km s^{-1}, and $\sigma_{v(BMR)} = 14$ km s^{-1}. The Sculptor dSph galaxy (Tolstoy et al. 2004) shows similar chemodynamic trends.

Figure 10 again illustrates that the velocity and metallicity of the stars in the WLM sample are changing with respect to position in the galaxy. The north field stars are more metal poor and have a higher approach velocity relative to the bar field stars. This chemodynamic signature is consistent with the interpretation of previous photometric studies that found a population gradient in WLM. However, our results separate the metallicity-velocity-position degeneracies, and we have also determined ages.

4.3. *Properties of Each Stellar Population and Comparisons to the Gas Dynamics*

The sample is divided into three age bins to examine the means and dispersions in the metallicities, velocities, ages, and elliptical radii of each stellar population, as listed in Table 4. Generally, the older stars are more metal poor and kinematically hotter than the younger stars. It should be stressed however, that the primary variations we see in our data are *radial* velocity and metallicity changes. This is confirmed unambiguously by a 4-d principal component analysis, and a k-means clustering analysis (see Leaman 2008 §4.5).

Of equal interest is the examination of the properties of the stars which do not show the same kinematic traits as the gas (from HI studies). The simplest expectation is that the metal rich stars would have formed from material that is more recently dynamically coupled to the gas, and would have had less time to become kinematically hot. This is borne out by the smaller velocity dispersion among the metal rich sub-sample of our dataset (see §4.2).

In addition to this, we can compare the stellar velocity gradient to that of the HI velocity gradient. Jackson et al. (2004) found an HI velocity gradient consistent with a rotation curve, and Kepley et al. (2007) derived a rotation velocity of ~ 30 km s^{-1} for the gas, with a more steeply varying velocity gradient in the northern approaching side of the galaxy. A direct comparison of the stellar and gas kinematics is shown in Figure 11, where the Kepley et al. (2007) HI position-velocity curve is overlaid on our stellar velocities. The average velocity separation between the flat central part of our stellar data and the approaching northern section is ~ 15 km s^{-1}. This is statistically significant given our errors of ± 6 km s^{-1} per star and error on the mean of $\pm$ 3 km s^{-1}. However the gradient is shallower and only half that of the gas rotation velocity. An apparent spatial lag is also seen, although the rotation center is consistent with the HI studies. These types of stellar and gas velocity discrepancies may be common in dwarf irregular galaxies, whether isolated or interacting, as witnessed by the massive star kinematics in the Small Magellanic Cloud reported by Evans & Howarth (2008)

Clearly the stellar members in this sample are not in the same velocity space as the bulk of the rotating gaseous component of WLM. In the northern part of the galaxy, the stars lag the gas rotation by as much as ~ 35 km s^{-1}. At the southern most part of our fields, the stars show a velocity offset of roughly the same magnitude, but opposite sign. To fully explain the complex velocity decoupling seen between the stellar and gaseous components of WLM will take a larger sample, but Figure 11 nicely illustrates the lack of coherent motion.

The parameter $\Delta V_{(star-gas)}$ has been calculated to quantify the difference in velocity of the stars from the gaseous components. For each star an offset in velocity was found by subtracting the stars' velocity from that of the gas velocity at the same right ascension and declination in WLM, according to an HI velocity map provided by Dr. A. Kepley (priv. comm.). This was done to search for subsamples of stars that track the gas velocity the closest. If the HI gas in WLM forms a thin rotating plane, then the youngest stars in our sample may track this better, than say, the oldest stars In Figure 12, $\Delta V_{(star-gas)}$ is plotted against v_{hel}, age, and metallicity. While there is some substructure in these representations, no clear trends emerge. This suggests that the stellar occupation of the HI velocity space is essentially random - that all stellar age bins/populations have been dynamically excited from the HI bulk motion. This would be consistent with the stellar population of WLM laying in a thick disk and/or spheroidal configuration. Even the youngest stars show a range in $\Delta V_{(star-gas)}$, thus either the gas and stars were never coupled (e.g., if the gas was recently accreted) or the mechanism responsible for dynamically decoupling the stellar velocities from the gas must have been present within the last few Gyr.

A bar in WLM's recent history could provide a natural explanation to the lack of coherent chemistry and ages amongst the stars that track the gas velocities the closest (recall Figure 11). Bars will dynamically stir a stellar population in a low mass galaxy such as WLM, and this also offers an explanation for the large velocity dispersions and velocity offsets in our sample when compared to the gas. Olsen & Massey (2007) noted tidal heating may be responsible for a dynamically hot component in the stellar disk of the LMC. However, given the isolation of WLM, a past bar may be a more feasible explanation for the dynamically hot component of WLM's stellar body.

Small scale HI features, including a bar, have been investigated by Kepley et al. (2007) and Jackson et al. (2004). Both identify a centrally evacuated region in the disk. Kepley et al. (2007) identify this as a ring or "hook" feature related to concentrated star formation and subsequent supernovae explosions, while Jackson et al. (2004) suggest either a central bar *or* a massive blowout region. Kepley et al. (2007) place an upper limit on the age of the ring at 128 Myr, which is much younger than the metal rich, young stars in our sample ($\leq$ 1.6 Gyr). However, these young stars also show a statistically significant peak in their radial velocity dispersion profile at the extent of the ring feature (see Leaman 2008). If these metal rich (and youngest) stars are responding dynamically to this feature, then this suggests the underlying physical mechanism is a resonance with longer term effects than sampled by the gas features alone. Interestingly, Kepley et al. (2007) estimate that as much as 20% of the total mass of WLM may be associated with this gas feature. While Kepley et al. (2007) note the HI isovelocity contours do not show the characteristic 's' shape of a bar, nor is the WLM IRAC data suggestive of one - the resonances affecting older stellar populations set up up by a past bar may outlive either of those indicators.

The ratio of rotation velocity to velocity dispersion ($\frac{v_{rot}}{\sigma_v}$) can provide information on the amount that a galaxy's structure is rotationally supported. In Table 5, we compare this ratio for our full sample of RGB stars, and various subpopulations. The stellar velocity ratio for the full sample is lower than that derived for the gas kinematics in Mateo (1998), although the gas velocity dispersion and the central density were assumed quantities. Our stellar rotational velocities were estimated by linearly fitting the heliocentric velocities versus elliptical radii. As expected, the metal poor, old, and "halo-like" subdivisions produce lower relative $\frac{v_{rot}}{\sigma_v}$ ratios than the other splits. These results suggest that the older stellar population in WLM is more pressure supported, while the younger stellar population (and gas) is more rotationally supported. While *all* of our stars lay off the plane occupied by the gas in position-velocity space, and appear dynamically excited and decoupled from the gas motion - we see a range of $\frac{v_{rot}}{\sigma_v}$ for the stellar subpopulations *within* that thick disk of stars itself.

While all of these results are intriguing, we stress that this work is limited by a very small statistical sample, particularly our last result since the older stars that suggest that stellar population is pressure supported rests on only 13 individual RGB stars with t $>$ 6 Gyr. A larger sample of stars is necessary to examine this and other results, and ultimately test the conditions of the isolated dwarf galaxies from the earliest epochs of star formation to the present. We have shown with this pilot survey that spectroscopic analysis of evolved WLM stars is possible, and with future observations on 8m class telesecopes we will be able to increase the sample size siginifcantly with additional fields.

5. SUMMARY

We have presented the first detailed analysis of the Ca II triplet spectra of 78 individual RGB stars in the isolated dwarf irregular galaxy WLM. Medium resolution spectra taken with the FORS2 spectrograph at the VLT in two fields in this galaxy (a central bar region, and a northern field) were coadded to improve the SNR $\geq$ 20. This is the first analysis of such faint RGB stars for *both* velocity and metallicity measurements, and therefore we have been especially careful in our data reduction techniques and error propagation calculations. The equivalent widths were converted into metallicities for each star using the calibration from Cole et al. (2004) with final errors $\sim \pm 0.25$ dex per star. The heliocentric velocities were determined to within ± 6 km s^{-1} (random error). Relative ages were derived from theoretical stellar evolution models, however differential extinction and evolutionary effects may bias our age distribution.

The north field and bar field metallicity distributions have mean metallicities and dispersions of [Fe/H]$= -1.45 \pm 0.04$, $\sigma = 0.33$ from 34 stars, and [Fe/H]$= -1.14 \pm 0.04$, $\sigma = 0.39$ from 44 stars, respectively. Both metallicity distributions are narrowly constrained with a range of approximately Δ[Fe/H]$\simeq$ 1.0. The stars in our sample show radial metallicity and velocity gradients, but interestingly the stellar rotation velocity is only approximately half that of the gas. The stellar velocities appear to be kinematically decoupled and in a thicker disk than the gas. Detailed comparisons with the HI gas, along with the isolation of WLM, suggest that the gas and stars were never coupled (e.g., recent HI infall) or that the stellar dynamics have been affected by resonances associated with a past bar.

WLM shows signatures of a metal poor population that is spatially and temporally distinct, and kinematically hotter than the young population at all radii - perhaps indicative of an extended halo. The velocities of the older stars suggest that this evolved stellar population in WLM is pressure supported, as opposed to the younger stars and gas disk which appear more rotationally supported. This latter result rests on a very small number of old RGB stars (13 with t $\geq$ 6 Gyr), but could have significant consequences for constraining theories of the structure and dynamics of dwarf galaxies in the early Universe. A larger sample and survey size is necessary to confirm these results and further characterize the stellar populations in WLM.

The authors thank Dr. Don VandenBerg for many useful discussions, and are grateful to Dr. Carme Gallart for many helpful comments on the original manuscript. We would like to thank Dr. Amanda Kepley for generously sharing her HI data. RL acknowledges support from NSERC Discovery Grants to DV and KV. RL also thanks SS for keeping him sane and grounded.

REFERENCES

Ables, H. D. & Ables, P. G. 1977, ApJS, 34, 245

Appenzeller, I., Fricke, K., Fürtig, W., Gässler, W., Häfner, R., Harke, R., Hess, H.-J., Hummel, W., Jürgens, P., Kudritzki, R.-P., Mantel, K.-H., Meisl, W., Muschielok, B., Nicklas, H., Rupprecht, G., Seifert, W., Stahl, O., Szeifert, T., & Tarantik, K. 1998, The Messenger, 94, 1

Armandroff, T. E. & Da Costa, G. S. 1991, AJ, 101, 1329

Barnes, D. G. & de Blok, W. J. G. 2004, MNRAS, 351, 333

Battaglia, G., Irwin, M., Tolstoy, E., Hill, V., Helmi, A., Letarte, B., & Jablonka, P. 2007, ArXiv e-prints, 710

—. 2008, MNRAS, 383, 183

Battaglia, G., Tolstoy, E., Helmi, A., Irwin, M. J., Letarte, B., Jablonka, P., Hill, V., Venn, K. A., Shetrone, M. D., Arimoto, N., Primas, F., Kaufer, A., Francois, P., Szeifert, T., Abel, T., & Sadakane, K. 2006, A&A, 459, 423

Battinelli, P. & Demers, S. 2004, A&A, 416, 111

Bosler, T. L., Smecker-Hane, T. A., & Stetson, P. B. 2007, MNRAS, 378, 318

Bresolin, F., Pietrzyński, G., Urbaneja, M. A., Gieren, W., Kudritzki, R.-P., & Venn, K. A. 2006, ApJ, 648, 1007

Brook, C., Richard, S., Kawata, D., Martel, H., & Gibson, B. K. 2007, ApJ, 658, 60

Carrera, R., Gallart, C., Hardy, E., Aparicio, A., & Zinn, R. 2007a, ArXiv e-prints, 710

Carrera, R., Gallart, C., Pancino, E., & Zinn, R. 2007b, AJ, 134, 1298

Carretta, E. & Gratton, R. G. 1997, A&AS, 121, 95

Cayrel, R. 1988, in IAU Symposium, Vol. 132, The Impact of Very High S/N Spectroscopy on Stellar Physics, ed. G. Cayrel de Strobel & M. Spite, 345–+

Cenarro, A. J., Cardiel, N., Gorgas, J., Peletier, R. F., Vazdekis, A., & Prada, F. 2001, MNRAS, 326, 959

Cenarro, A. J., Gorgas, J., Cardiel, N., Vazdekis, A., & Peletier, R. F. 2002, MNRAS, 329, 863

Cole, A. A., Grocholski, A. J., Geisler, D., Sarajedini, A., Smith, V. V., & Tolstoy, E. 2008, in IAU Symposium, Vol. 256, The Magellanic System: Star, Gas and Galaxies, ed. J. T. van Loon & J. M. Oliveira

Cole, A. A., Smecker-Hane, T. A., Tolstoy, E., Bosler, T. L., & Gallagher, J. S. 2004, MNRAS, 347, 367

Cole, A. A., Tolstoy, E., Gallagher, III, J. S., & Smecker-Hane, T. A. 2005, AJ, 129, 1465

Demers, S., Battinelli, P., & Artigau, E. 2006, A&A, 456, 905

Dolphin, A. E. 2000, ApJ, 531, 804

Evans, C. J. & Howarth, I. D. 2008, MNRAS, 386, 826

Gallouet, L., Heidmann, N., & Dampierre, F. 1975, A&AS, 19, 1

Gieren, W., Pietrzyński, G., Szewczyk, O., Soszyński, I., Bresolin, F., Kudritzki, R.-P., Urbaneja, M. A., Storm, J., & Minniti, D. 2008, ApJ, 683, 611

Gnedin, N. Y. & Kravtsov, A. V. 2006, ApJ, 645, 1054

Grocholski, A. J., Cole, A. A., Sarajedini, A., Geisler, D., & Smith, V. V. 2006, AJ, 132, 1630

Harris, W. E. 1996, AJ, 112, 1487

Hodge, P. & Miller, B. W. 1995, ApJ, 451, 176

Hodge, P. W., Dolphin, A. E., Smith, T. R., & Mateo, M. 1999, ApJ, 521, 577

Huchtmeier, W. K., Seiradakis, J. H., & Materne, J. 1981, A&A, 102, 134

Jackson, D. C., Skillman, E. D., Cannon, J. M., & Côté, S. 2004, AJ, 128, 1219

Jackson, D. C., Skillman, E. D., Gehrz, R. D., Polomski, E., & Woodward, C. E. 2007, ApJ, 656, 818

Jorgensen, U. G., Carlsson, M., & Johnson, H. R. 1992, A&A, 254, 258

Kaufmann, T., Mayer, L., Wadsley, J., Stadel, J., & Moore, B. 2007, MNRAS, 375, 53

Kepley, A. A., Wilcots, E. M., Hunter, D. A., & Nordgren, T. 2007, AJ, 133, 2242

Koch, A., Grebel, E. K., Wyse, R. F. G., Kleyna, J. T., Wilkinson, M. I., Harbeck, D. R., Gilmore, G. F., & Evans, N. W. 2006, AJ, 131, 895

Leaman, R. 2008, Master's thesis, University of Victoria, Canada

Lee, H., Skillman, E. D., & Venn, K. A. 2005, ApJ, 620, 223

Madau, P., Ferrara, A., & Rees, M. J. 2001, ApJ, 555, 92

Mateo, M. L. 1998, ARA&A, 36, 435

Mayer, L., Mastropietro, C., Wadsley, J., Stadel, J., & Moore, B. 2006, MNRAS, 369, 1021

McConnachie, A. W., Irwin, M. J., Ferguson, A. M. N., Ibata, R. A., Lewis, G. F., & Tanvir, N. 2005, MNRAS, 356, 979

McConnachie, A. W., Venn, K. A., Irwin, M. J., Young, L. M., & Geehan, J. J. 2007, ApJ, 671, L33

Minniti, D. & Zijlstra, A. A. 1997, AJ, 114, 147

Moore, B., Ghigna, S., Governato, F., Lake, G., Quinn, T., Stadel, J., & Tozzi, P. 1999, ApJ, 524, L19

Navarro, J. F., Frenk, C. S., & White, S. D. M. 1997, ApJ, 490, 493

Olsen, K. A. G. & Massey, P. 2007, ApJ, 656, L61

Osterbrock, D. E. & Martel, A. 1992, PASP, 104, 76

Pont, F., Zinn, R., Gallart, C., Hardy, E., & Winnick, R. 2004, AJ, 127, 840

Rejkuba, M., Minniti, D., Gregg, M. D., Zijlstra, A. A., Alonso, M. V., & Goudfrooij, P. 2000, AJ, 120, 801

Ricotti, M. & Gnedin, N. Y. 2005, ApJ, 629, 259

Rutledge, G. A., Hesser, J. E., & Stetson, P. B. 1997, PASP, 109, 907

Skillman, E. D., Terlevich, R., & Melnick, J. 1989, MNRAS, 240, 563

Stetson, P. B. 1994, PASP, 106, 250

Tolstoy, E. 2003, in Astronomical Society of the Pacific Conference Series, Vol. 296, New Horizons in Globular Cluster Astronomy, ed. G. Piotto, G. Meylan, S. G. Djorgovski, & M. Riello, 234–+

Tolstoy, E., Irwin, M. J., Cole, A. A., Pasquini, L., Gilmozzi, R., & Gallagher, J. S. 2001, MNRAS, 327, 918

Tolstoy, E., Irwin, M. J., Helmi, A., Battaglia, G., Jablonka, P., Hill, V., Venn, K. A., Shetrone, M. D., Letarte, B., Cole, A. A., Primas, F., Francois, P., Arimoto, N., Sadakane, K., Kaufer, A., Szeifert, T., & Abel, T. 2004, ApJ, 617, L119

Tolstoy, E., Venn, K. A., Shetrone, M., Primas, F., Hill, V., Kaufer, A., & Szeifert, T. 2003, AJ, 125, 707

Urbaneja, M. A., Kudritzki, R. ., Bresolin, F., Przybilla, N., Gieren, W., & Pietrzynski, G. 2008, ArXiv e-prints, 805

van den Bergh, S. 1994, AJ, 107, 1328

VandenBerg, D. A., Bergbusch, P. A., & Dowler, P. D. 2006, ApJS, 162, 375

Venn, K. A. & Hill, V. M. 2008, The Messenger, 134, 23

Venn, K. A., Irwin, M., Shetrone, M. D., Tout, C. A., Hill, V., & Tolstoy, E. 2004, AJ, 128, 1177

Venn, K. A., Tolstoy, E., Kaufer, A., Skillman, E. D., Clarkson, S. M., Smartt, S. J., Lennon, D. J., & Kudritzki, R. P. 2003, AJ, 126, 1326

Whiting, A. B., Hau, G. K. T., & Irwin, M. 1999, AJ, 118, 2767

Youngblood, A. J. & Hunter, D. A. 1999, ApJ, 519, 55

Zinn, R. & West, M. J. 1984, ApJS, 55, 45

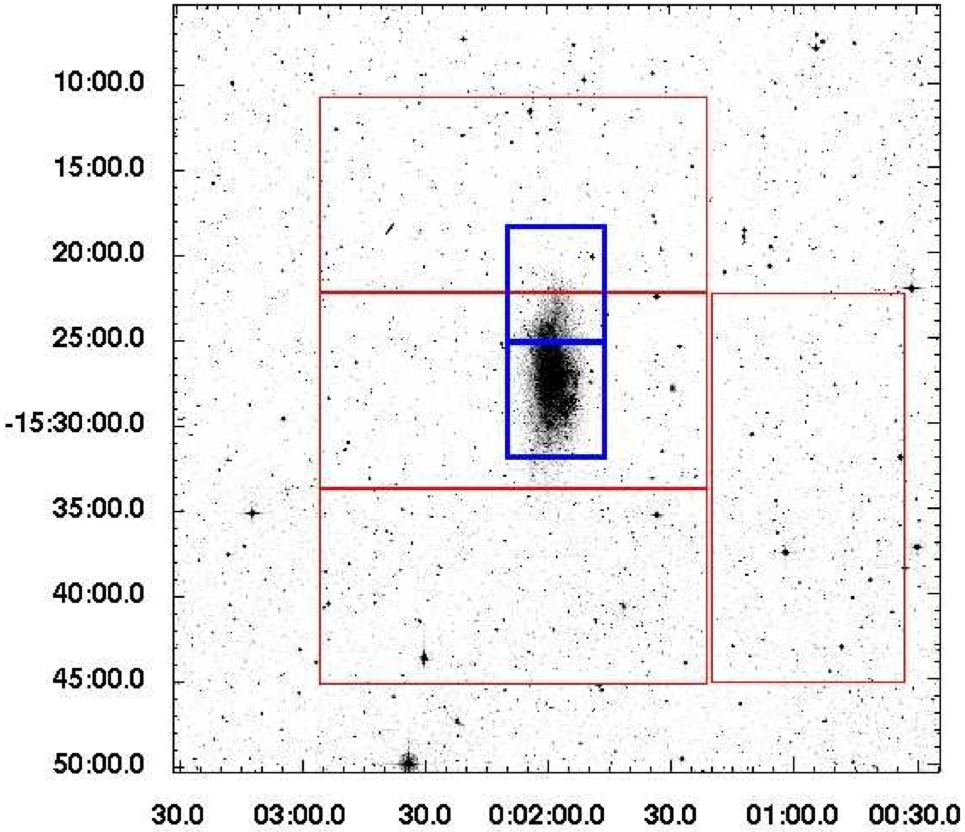

FIG. 1.— Digitized Sky Survey SERC-J image of WLM. The total image is approximately $45' \times 45'$, with North being up and East to the left. The relative locations of the north and bar fields (*blue*) from this FORS2 spectroscopic work are shown. The four red boxes indicate the fields imaged by the INT WFC survey (see McConnachie et al. 2005) The two A-type supergiants from Venn et al. (2003) are located approximately in the centre of our bar field, along with the HII regions from Hodge & Miller (1995), and the B supergiants from Bresolin et al. (2006).

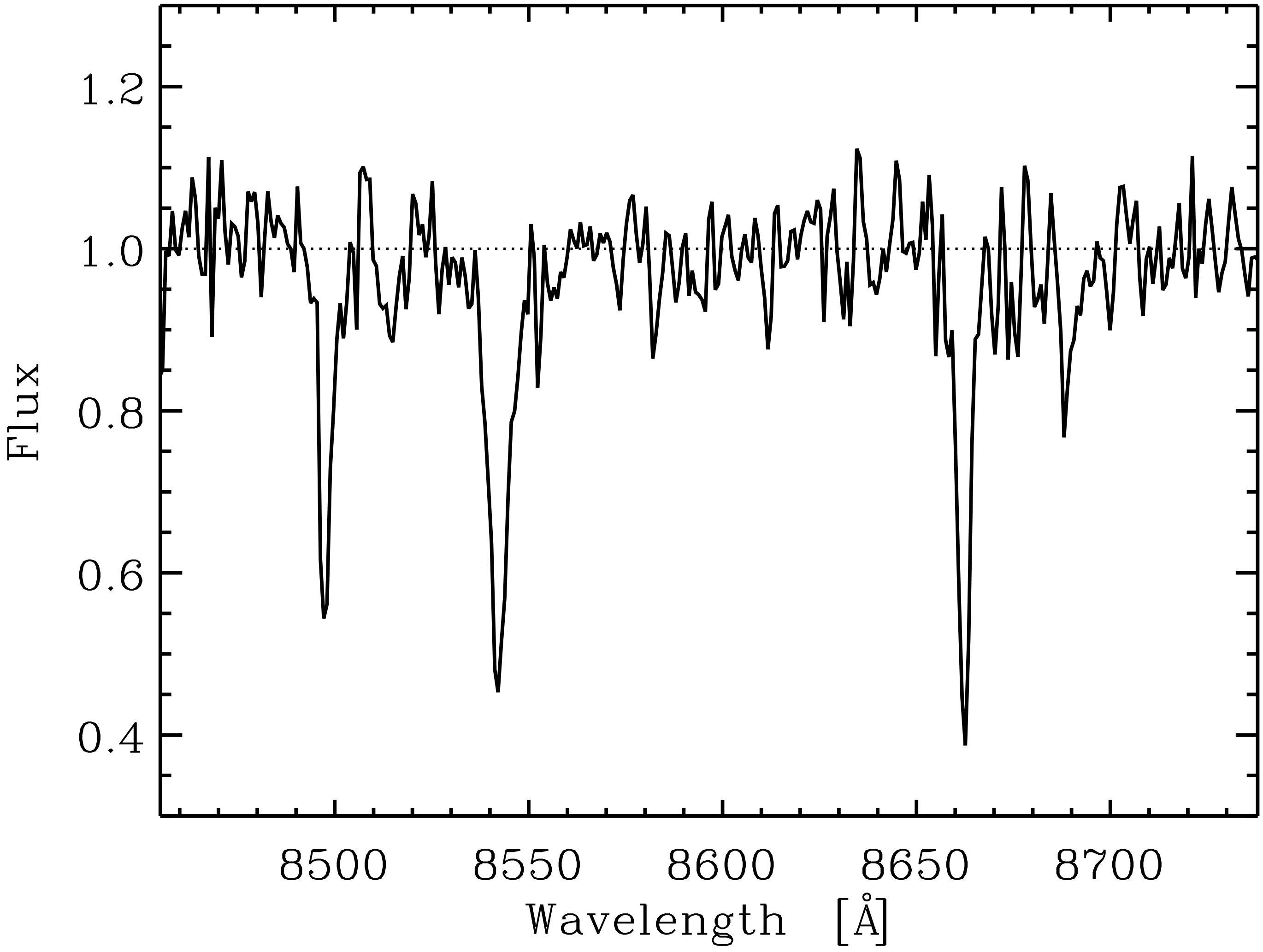

FIG. 2.— Sample combined spectra for one star (STARID 28531) in the WLM FORS2 north field (*top left*). The prominent calcium absorption features are visible at $\lambda\lambda \sim 8498$Å, 8542Å, and 8662 Å even in this (S/N)$\sim$22 image. The y-axis are relative flux units. A dotted line has been drawn at the global continuum level of unity.

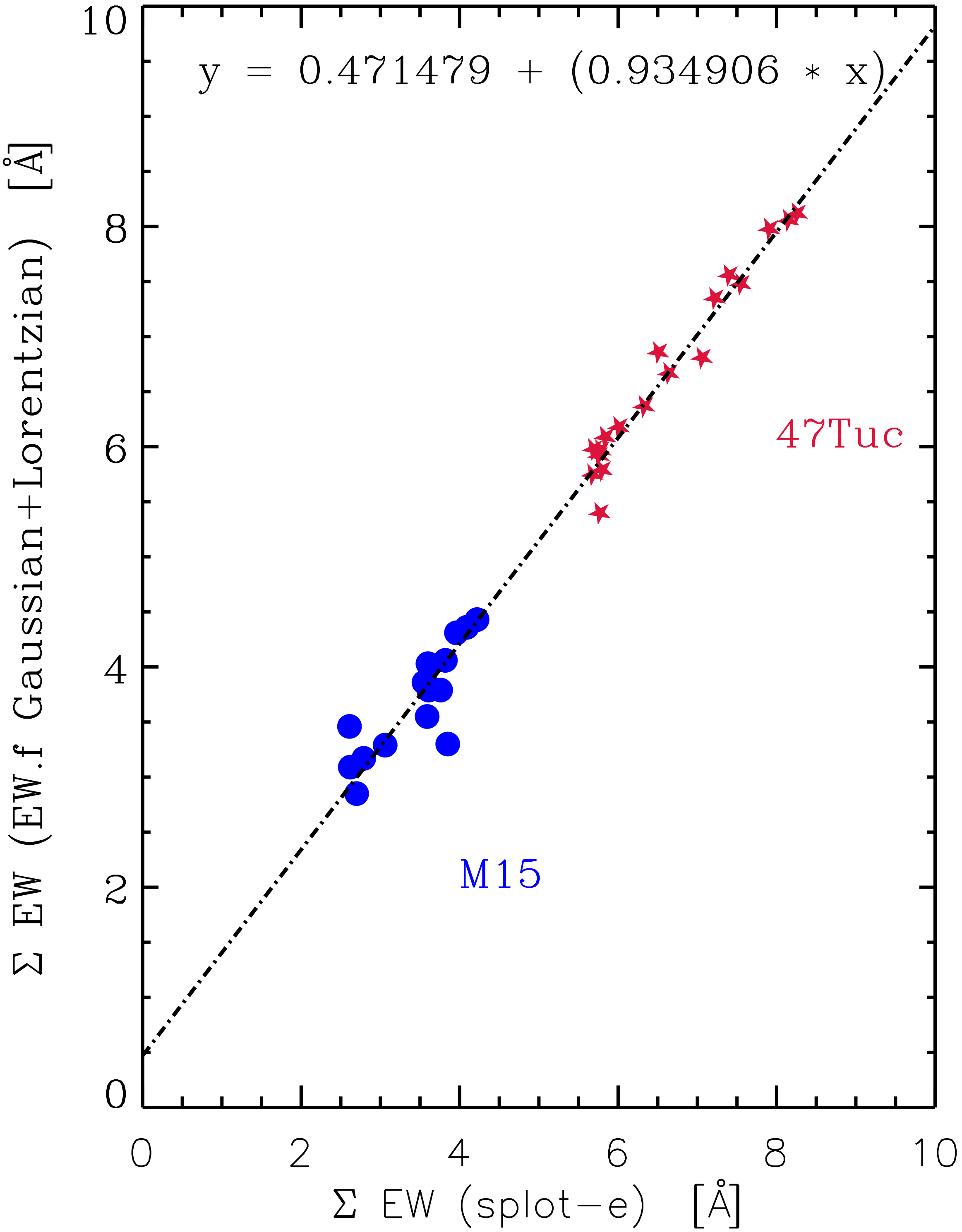

Fig. 3.— Comparison of ΣEW measurements using the pixel integration method described in this work, and the Gaussian + Lorentzian profile fits from Cole et al. (2004), for two extreme metal poor and rich calibrating galactic globular clusters. The results of a global linear least squares fit to the two cluster stars is shown as the dot dashed line. The rms dispersion about the fit is 0.22 Å.

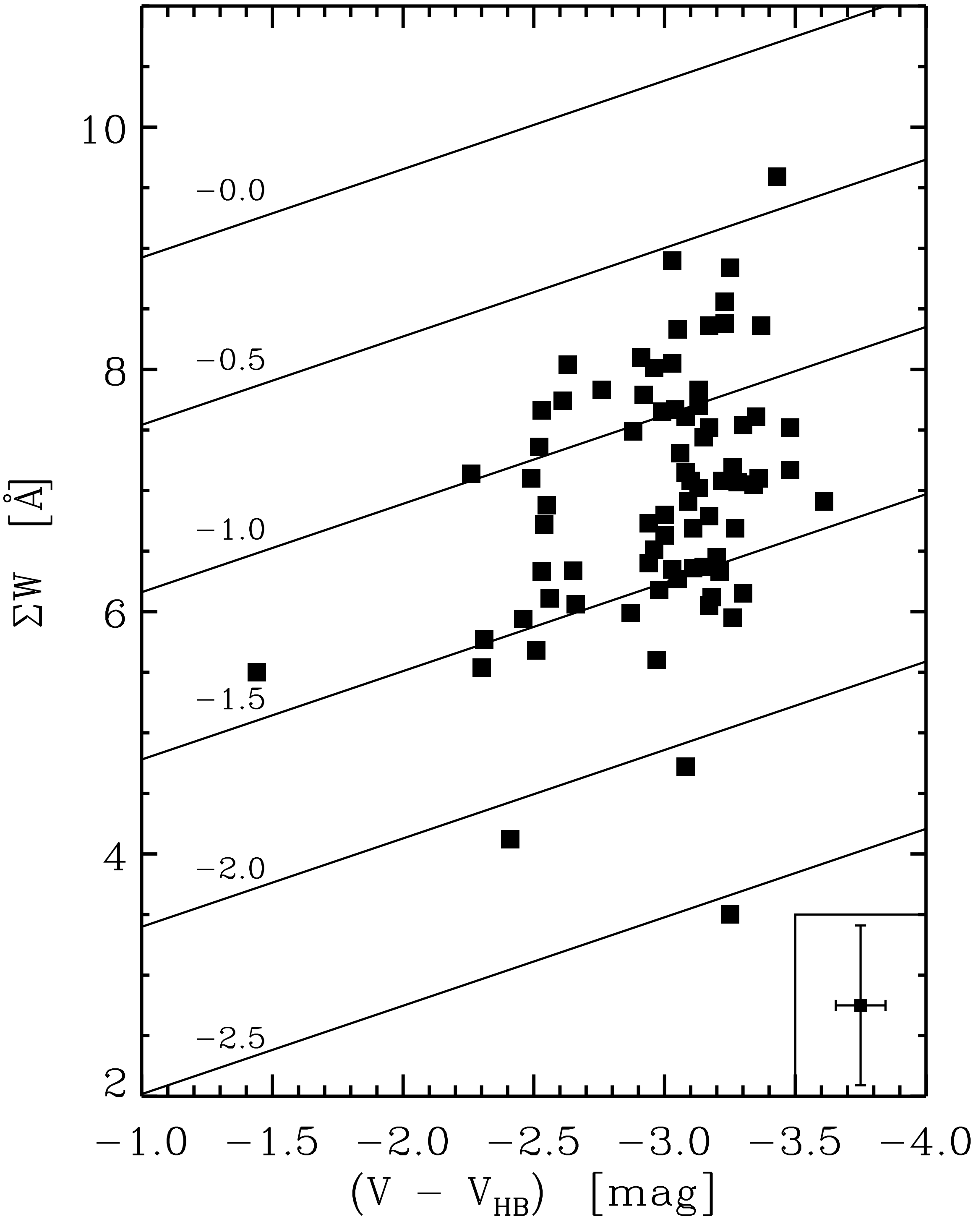

FIG. 4.— Summed equivalent width of the Calcium II triplet lines (ΣW) versus the V magnitude above the horizontal branch. The solid lines show constant metallicity according to the calibration by Cole et al. (2004) which we used to derive our final [Fe/H] values (see text).

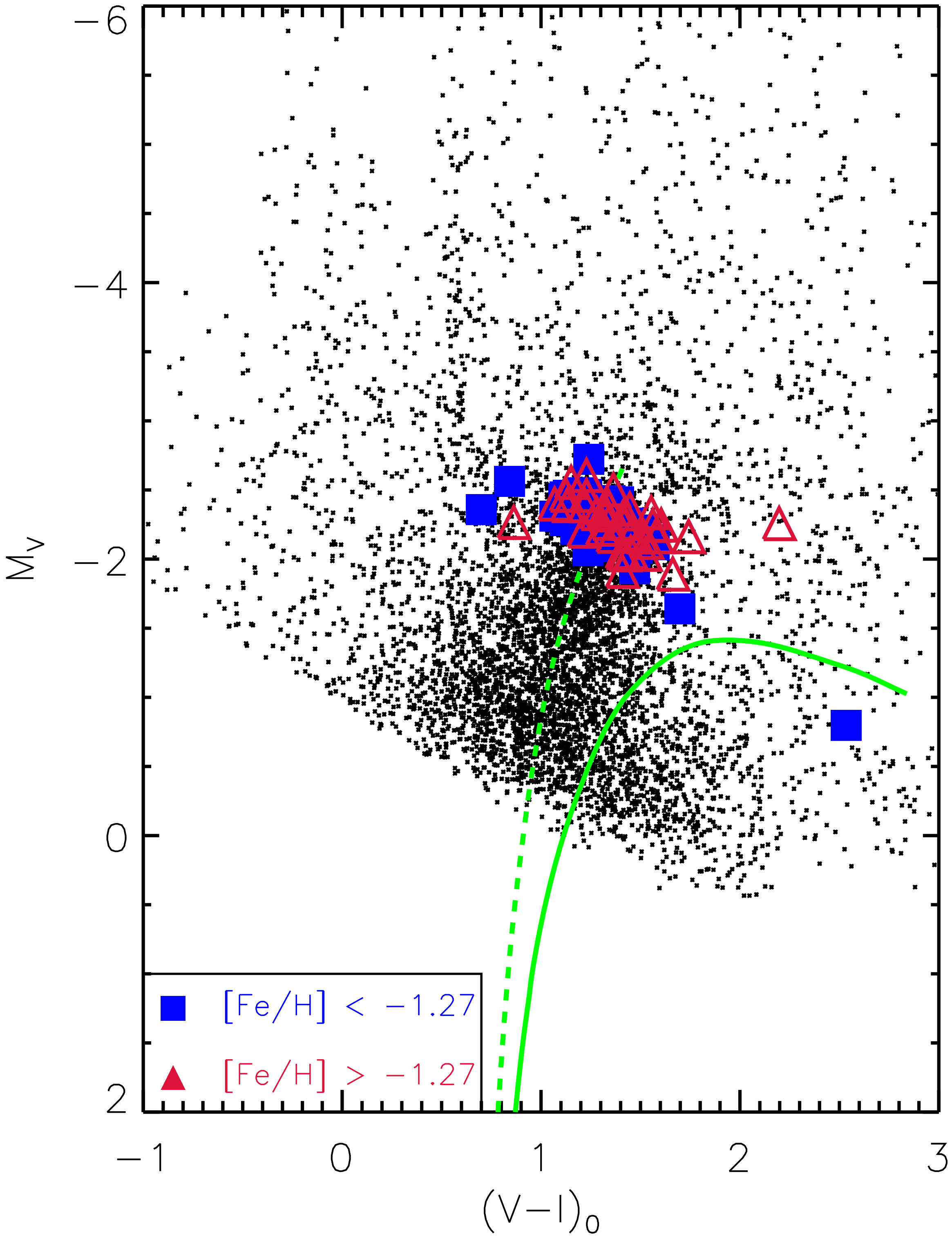

Fig. 5.— CMD of target stars with [Fe/H] ≤ −1.27 (*blue boxes*) and ≥ -1.27 (*red triangles*) with the fiducial sequences for 47 Tuc ([Fe/H] ∼ -0.7) and M68 ([Fe/H]∼ -2.0 *green dashed line*). The full catalogue of INT WFC photometry is shown as the black dots. It can be seen that there are both metal poor and metal rich stars blueward of the fiducial sequence for M68. This indicates that we are most likely sampling a younger population in some areas. More information on age trends can be found in §4.1.

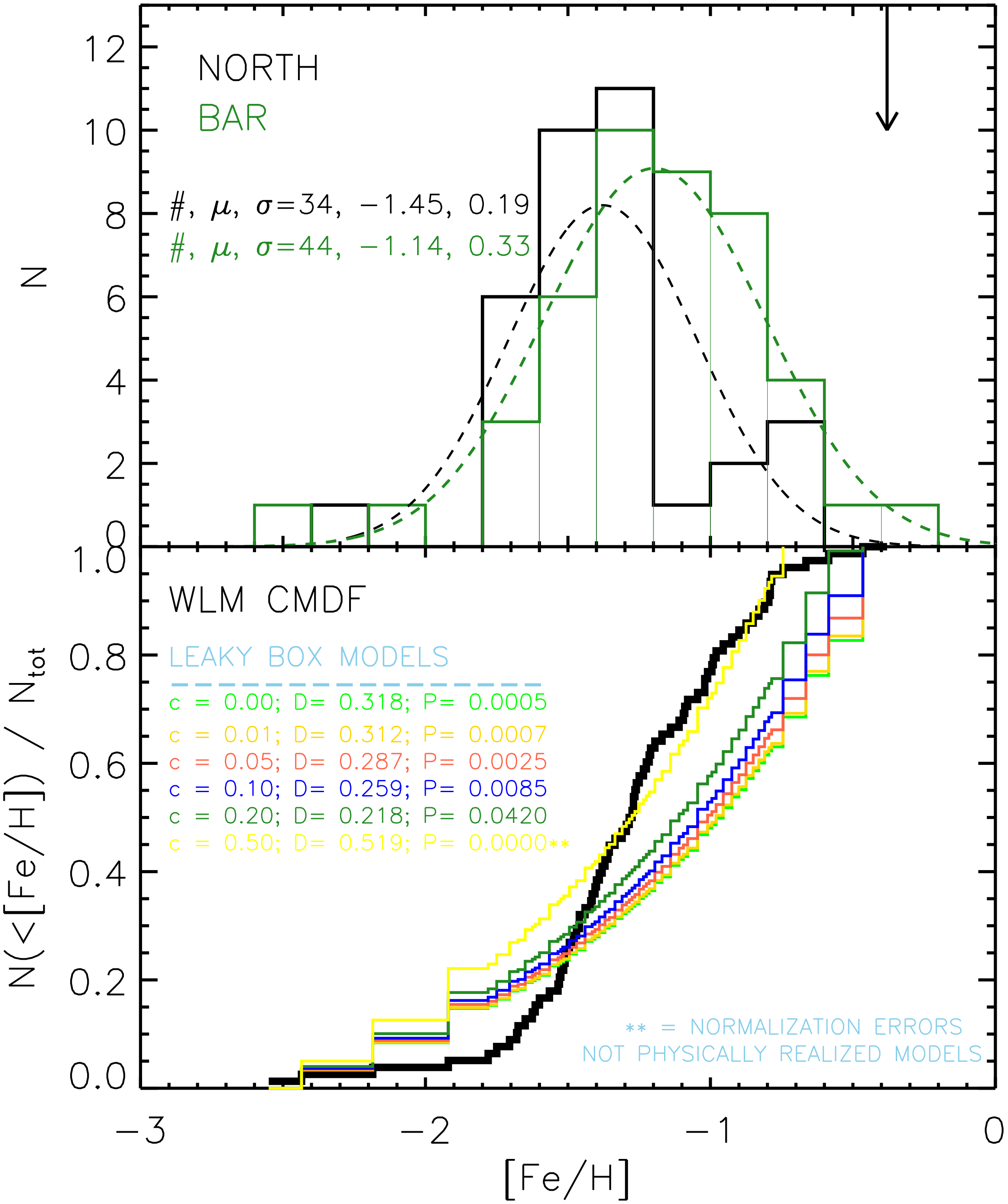

Fig. 6.— The metallicity distribution function for the two FORS2/MXU fields in WLM (*top panel*). The bin size is 0.2 dex, and fitted Gaussians with parameters shown are indicated by the dashed lines. Note that the mean values for the two fields differ by ∼ 0.3 dex, and there is an absence of extreme or even moderately metal poor stars in either field. The [Fe/H] estimates from the Venn et al. (2003) supergiants are shown by the solid arrow. The cumulative metallicity distribution function (unbinned) for our WLM sample is shown in the bottom panel. The coloured lines represent cumulative distributions for simple leaky box chemical evolution models, with different values (c) controlling the effective yield). Corresponding Kolmogorov-Smirnov D-statistics (D), and probabilities (P) are shown as well.

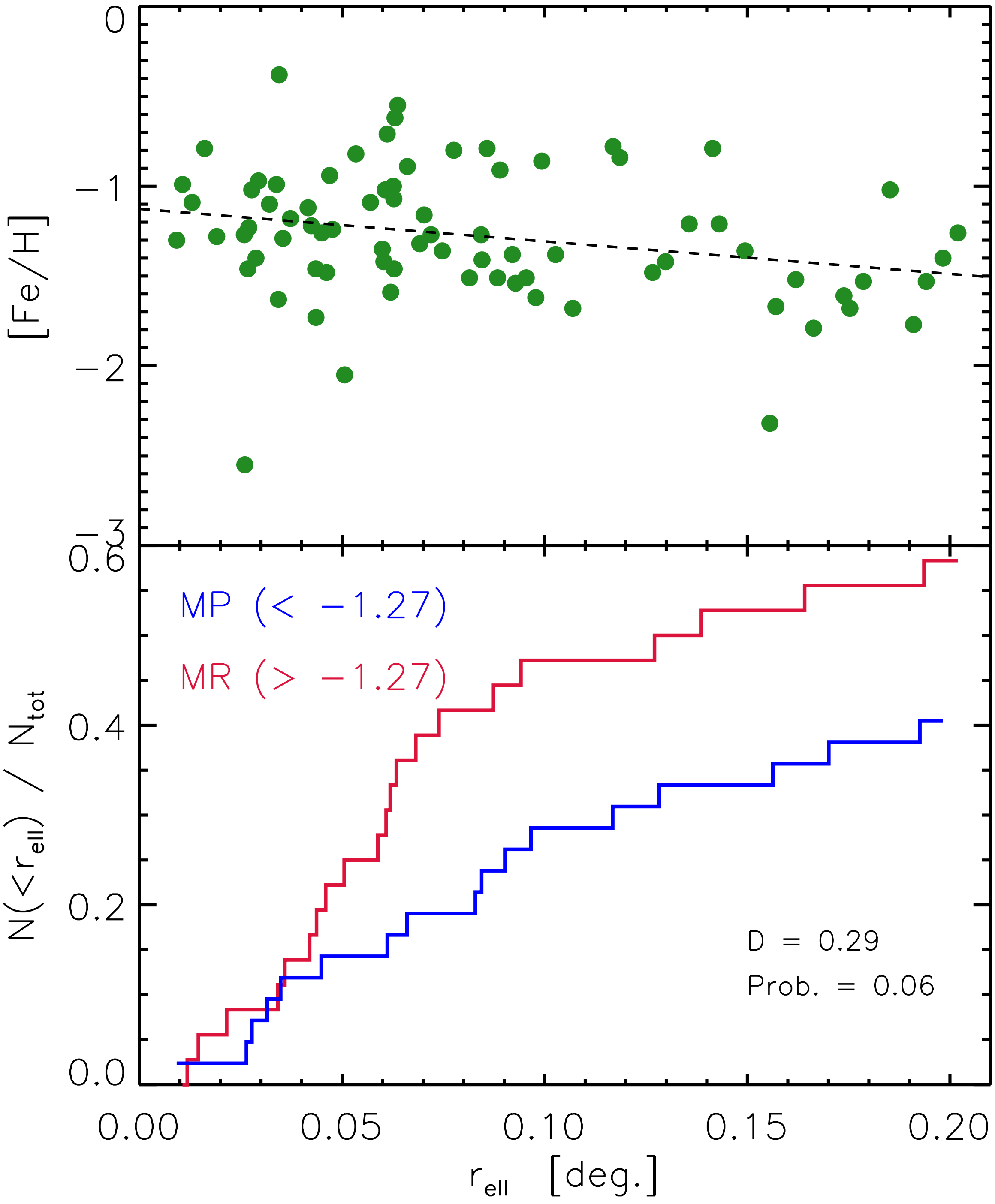

Fig. 7.— [Fe/H] vs. elliptical radii for the full sample of RGB stars in WLM (*top panel*). A radial change is clearly evident, and quantitatively confirms the interpretation of the disk of WLM being a region of higher SF in more recent times relative to the outer galactic regions. Cumulative distribution functions vs. elliptical radii for the metal rich and metal poor subsamples (*bottom panel*). The metal poor half of the sample rises more linearly over the radial extent of our survey, compared to the more centrally concentrated metal rich subpopulation. Shown are the K-S D statistic, and probability for a two sided K-S test of the two distributions.

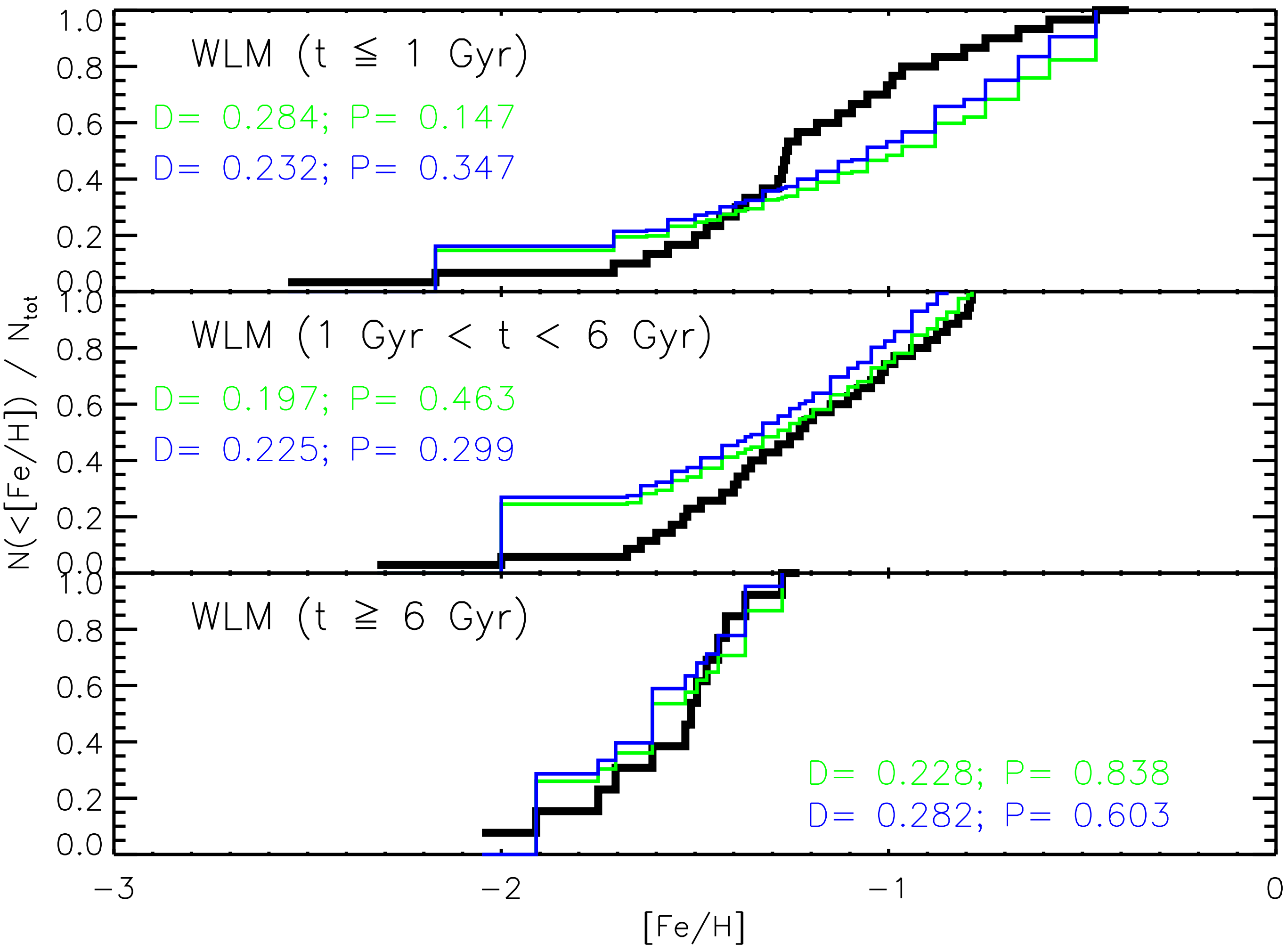

FIG. 8.— Cumulative metallicity distributions for our WLM sample, subdivided by ages: $t < 1$ Gyr (*top panel*), $1 \leq t \leq 6$ (*middle panel*), $t > 6$ Gyr (*bottom panel*). Comparison CDFs based on simple closed (*green*), and leaky box (*blue*) chemical evolution models are shown for each age set. The two sided Kolmogorov-Smirnov D statistics are shown, as well as the probability that our metallicity distributions are drawn from one of the theoretical distributions. The probability rises steeply with age for the closed box model, with $P \sim 14\%, 46\%, 84\%$ in the three bins.

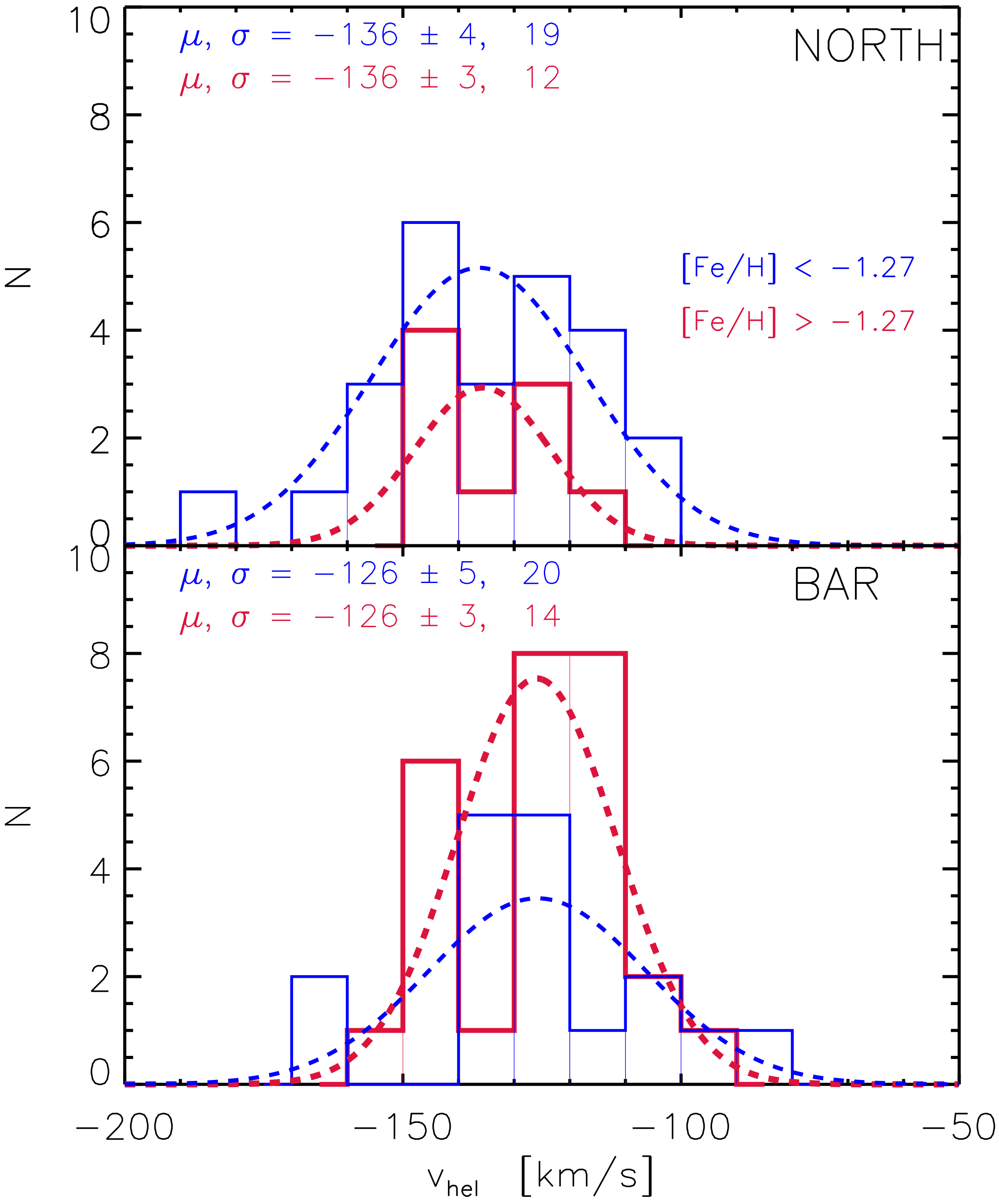

FIG. 9.— Velocity distributions for metallicity segregated subsamples in the north field (*top panel*), and the bar field (*bottom panel*). The average metallicity and dispersion values from the Gaussian fits (*dashed lines*) are shown for all stars in each field near the top of each panel. The mean uncertainty for each heliocentric corrected radial velocity value was ±6 km s^{-1}.

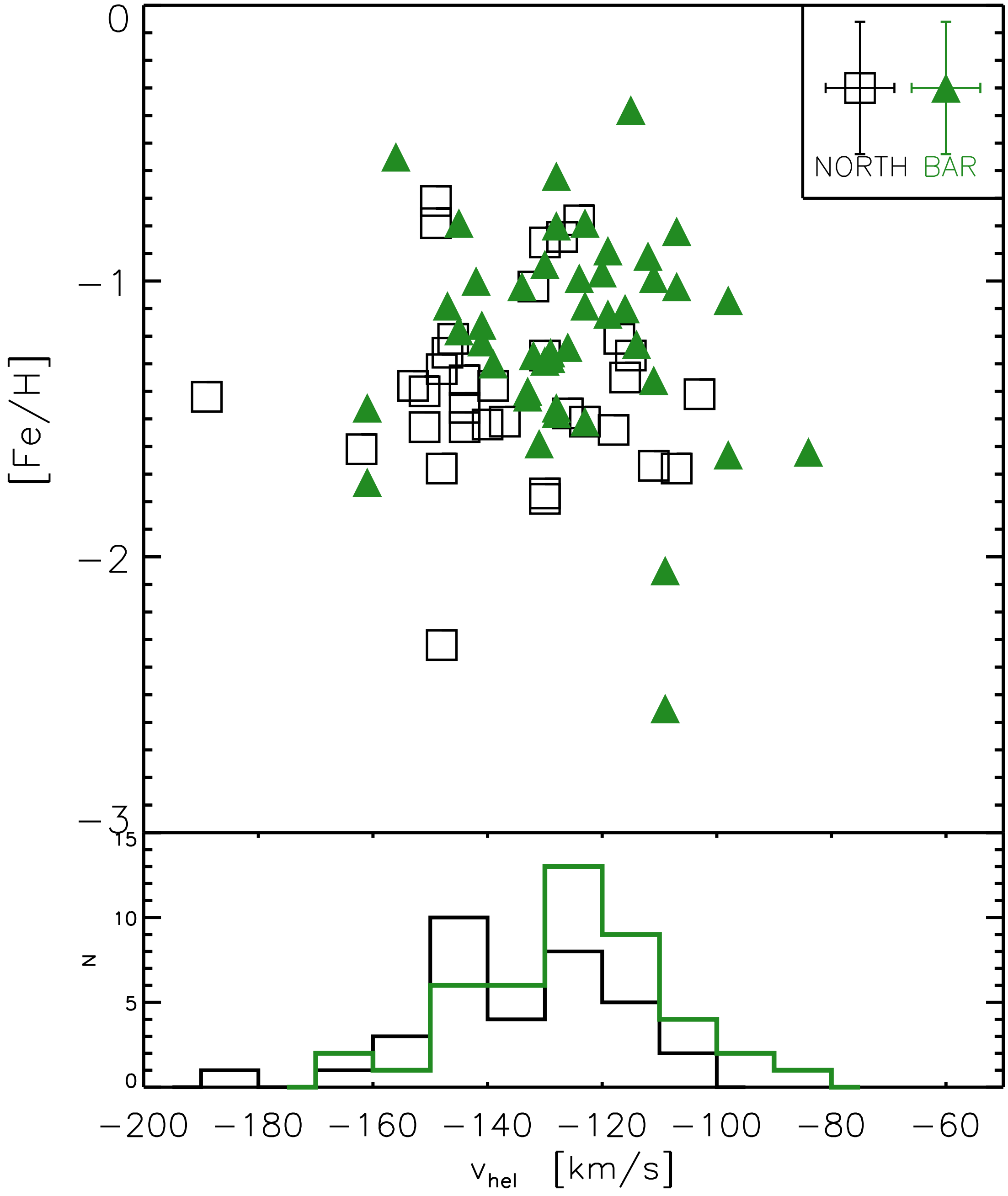

FIG. 10.— Plot of the heliocentric velocity and metallicity of the 78 RGB stars in our two WLM fields. The mean bar(*green triangles*) and north (*open squares*) field values are noticeably offset in both chemical and velocity space. The velocity offset between the two fields is shown more clearly by the histogram in the subpanel. Errors are ±0.25 dex, and ±6 km s^{-1} respectively per star, and shown for comparison on the simulated legend points at the top.

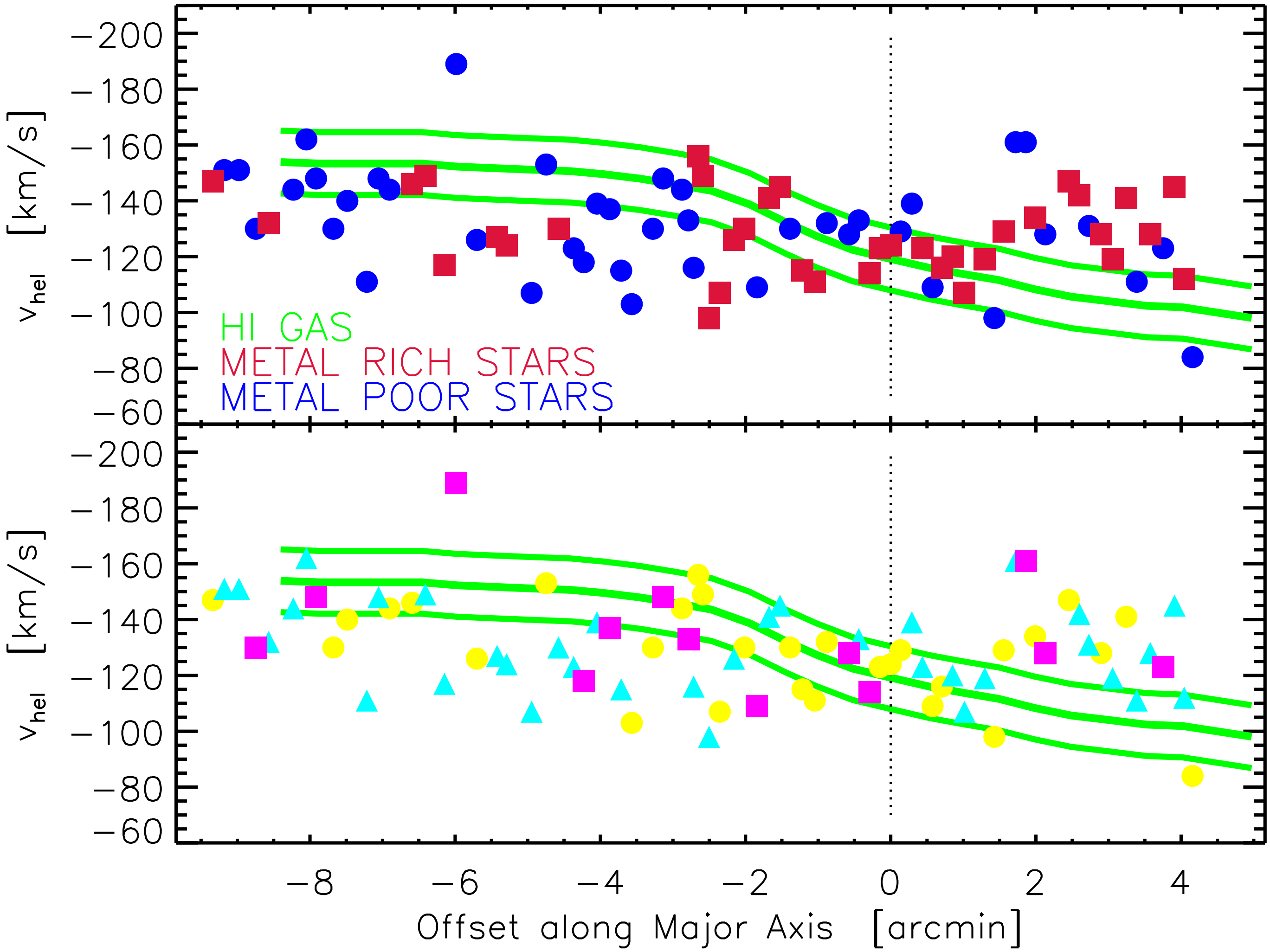

FIG. 11.— (*top panel*) Comparison of the heliocentric stellar velocity data for the metal rich (red), metal poor (blue) WLM subpopulations. Shown in green is the Kepley et al. (2007) HI gas position-velocity curve. Neither subpopulation tracks the gas particularly well, and the velocity gradient is only half that seen for the HI data (see text). (*bottom panel*) Similar visualization, but with the WLM stars subdivided into three age bins: $t \leq 1$ Gyr (*circles*), $1 \leq t \leq 6$Gyr (*triangles*), $t \geq 6$ Gyr (*squares*). Negative offsets along the major axis correspond to the north portion of the galaxy, postive offsets the southern direction.

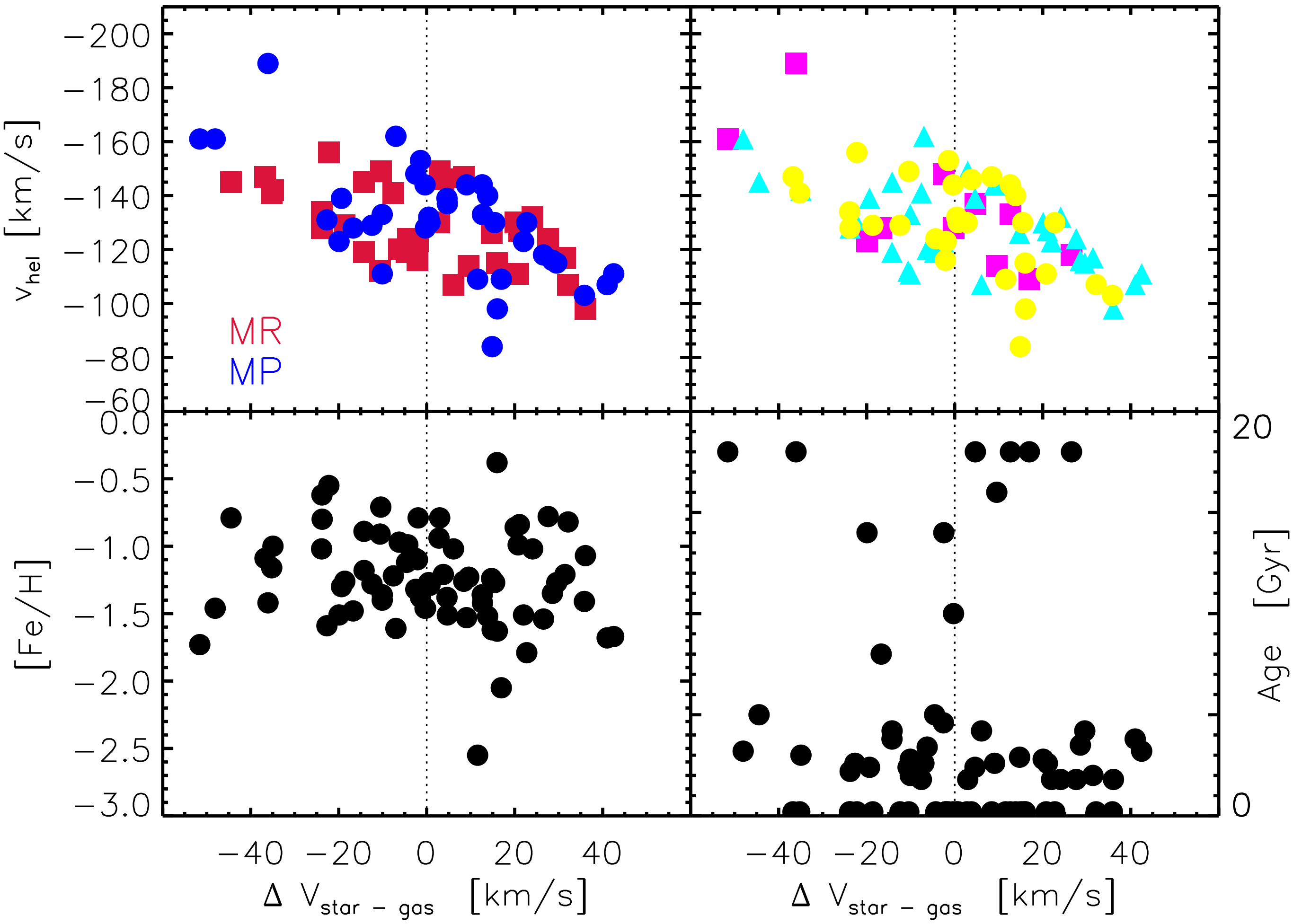

FIG. 12.— Shown is the stellar to gas velocity offset (see text) for all stars in our sample, compared against various parameters. Upper panels show the $\Delta V_{(star-gas)}$ values versus v_{hel} for metallicity bins, and age bins (symbols are the same as in Figure 11). (*bottom panels*) $\Delta V_{(star-gas)}$ plotted versus [Fe/H] and age. No clear trend exists between the star-gas velocity offset and the metallicity or age values.

TABLE 1
WLM PROPERTIES

Quantity	Value	Reference
(l, b)	(75.85, -73.63)	Gallouet et al. (1975)
E(B-V)	0.035 (mag.)	McConnachie et al. (2005)
Distance	932 ± 33 kpc	McConnachie et al. (2005)
Eccentricity	0.59	Ables & Ables (1977)
Position Angle	181 (deg.)	Jackson et al. (2004)
Heliocentric Velocity (v_{hel}^{HI})	-130 km s^{-1}	Jackson et al. (2004)
Rotation Velocity (v_{rot}^{HI})	30 km s^{-1}	Kepley et al. (2007)
$\mathrm{M_v}$	14.1 (mag.)	van den Bergh (1994)
M_{dyn}	$2.16 \times 10^9 M_\odot$	Kepley et al. (2007)
M_{HI}	$(6.3 \pm 0.3) \times 10^7 M_\odot$	Kepley et al. (2007)
$[Fe/H]_{phot}^{RGB}$	-1.45 ± 0.2 dex	Minniti & Zijlstra (1997)

TABLE 2
Observational Parameters

Target	Mag. Range	Distance (kpc)	R.A.	Dec.	Exp. Time (minutes)
WLM-N	$22.1 \leq V_{mag} \leq 24.0$	970[a]	00:01:58	-15:21:47	320
WLM-B	$22.2 \leq V_{mag} \leq 23.2$	970[a]	00:01:58	-15:28:30	320
NGC 104	$11 \leq V_{mag} \leq 14$	4.5	00:24:05	-72:04:51	1
NGC 1851	$12 \leq V_{mag} \leq 16$	12.1	05:14:06	-40:02:50	1
NGC 1904	$12 \leq V_{mag} \leq 16$	12.9	05:24:10	-24:31:27	1
NGC 7078	$12 \leq V_{mag} \leq 16$	10.3	21:29:58	+12:10:01	1

Note. — The location and distance data for the four calibrating globular clusters is taken from the Harris (1996) catalogue which can be found online at http://physwww.mcmaster.ca/~harris/mwgc.dat

[a] From Gieren et al. (2008)

TABLE 3
Selected Parameters For WLM Stellar Sample

STARID	R.A. (degrees)	Dec. (degrees)	r_{ell} (degrees)	V (mag.)	I (mag.)	W_1 (Å)	W_2 (Å)	W_3 (Å)	$[Fe/H]_{CaT}$ (dex)	Δ[Fe/H] (dex)	V_{hel} (km s^{-1})	ΔV_{hel} (km s^{-1})	Age [a] (Gyr)
27626	0.5293	-15.5334	0.0978074	22.54	21.43	1.076	2.108	2.781	-1.62	0.21	-84	7	$\leq$ 1.6
28986	0.4753	-15.5315	0.0889742	22.82	21.36	1.209	3.408	3.208	-0.91	0.26	-112	8	2.4
29674	0.4773	-15.5292	0.0857606	22.96	21.25	1.250	3.316	3.527	-0.79	0.27	-145	9	5.0
28080	0.4978	-15.5266	0.0814584	22.64	21.09	1.072	2.972	2.158	-1.51	0.22	-123	6	14.0
28895	0.4971	-15.5237	0.0775812	22.80	21.35	1.551	3.819	2.791	-0.80	0.27	-128	7	2.2
27491	0.5058	-15.5205	0.0747572	22.51	21.19	1.255	2.680	2.821	-1.36	0.23	-111	7	2.0
26541	0.4892	-15.5182	0.0702356	22.25	20.97	1.604	3.500	2.439	-1.16	0.25	-141	7	$\leq$ 1.6
27842	0.4915	-15.5150	0.0661231	22.59	20.35	1.332	3.647	3.089	-0.89	0.27	-119	7	3.8
27409	0.4978	-15.5124	0.0630628	22.49	21.00	1.643	3.800	3.509	-0.62	0.28	-128	7	$\leq$ 1.6
27569	0.4726	-15.5096	0.0620014	22.53	21.22	1.032	2.836	2.177	-1.59	0.21	-131	6	2.6
27916	0.4639	-15.5074	0.0626483	22.61	20.96	1.735	3.463	2.533	-1.00	0.25	-142	7	3.0
27018	0.4707	-15.5049	0.0569988	22.39	21.12	1.284	3.317	3.305	-1.09	0.25	-147	7	$\leq$ 1.6
27845	0.4883	-15.4996	0.0461610	22.59	21.10	1.351	3.373	1.615	-1.48	0.22	-128	6	8.0
28137	0.5336	-15.4972	0.0606404	22.65	21.39	1.065	4.178	2.393	-1.02	0.26	-134	8	$\leq$ 1.6
28441	0.5078	-15.4951	0.0435499	22.71	21.12	0.860	2.543	2.087	-1.73	0.20	-161	9	18.0
28427	0.4690	-15.4927	0.0435044	22.71	21.37	1.318	3.107	1.863	-1.46	0.22	-161	6	3.2
27310	0.4617	-15.4900	0.0449992	22.46	21.29	1.502	3.167	2.398	-1.26	0.24	-129	7	$\leq$ 1.6
26940	0.4765	-15.4879	0.0342952	22.37	21.13	1.307	3.107	1.655	-1.63	0.22	-98	7	$\leq$ 1.6
28333	0.4608	-15.4856	0.0416024	22.69	21.14	0.996	3.479	2.841	-1.12	0.25	-119	6	5.0
28970	0.5081	-15.4810	0.0277182	22.82	21.25	1.38	3.03	3.097	-1.02	0.25	-107	6	4.2
28881	0.5140	-15.4783	0.0293921	22.80	21.31	1.269	3.353	3.056	-0.97	0.26	-120	7	3.4
27265	0.5193	-15.4758	0.0320861	22.45	21.34	1.295	3.567	2.699	-1.10	0.25	-116	6	$\leq$ 1.6
27427	0.4687	-15.4737	0.0260121	22.49	21.75	0.971	1.304	0.962	-2.55	0.13	-109	9	$\leq$ 1.6
27926	0.4824	-15.4713	0.0129957	22.61	21.00	1.505	3.346	2.603	-1.09	0.25	-123	6	4.6
28395	0.4847	-15.4689	0.0091797	22.70	21.41	1.213	3.563	1.996	-1.30	0.24	-139	6	2.4
26678	0.5100	-15.4664	0.0190786	22.29	21.40	0.977	3.412	2.772	-1.28	0.25	-129	5	$\leq$ 1.6
27833	0.5018	-15.4641	0.0106341	22.59	21.68	1.572	3.131	3.069	-0.99	0.25	-124	6	$\leq$ 1.6
27429	0.5069	-15.4616	0.0160755	22.49	21.13	1.703	3.674	3.058	-0.79	0.27	-123	7	$\leq$ 1.6
28322	0.4653	-15.4592	0.0269871	22.69	20.90	1.640	2.952	2.410	-1.23	0.23	-114	6	16.0
27407	0.5182	-15.4567	0.0287657	22.49	21.11	1.358	3.259	2.033	-1.40	0.23	-133	7	2.8
28405	0.5148	-15.4545	0.0267520	22.70	21.18	1.132	2.586	2.590	-1.46	0.22	-128	6	10.0
27044	0.5086	-15.4494	0.0258708	22.40	21.24	1.241	3.385	2.467	-1.27	0.24	-132	6	$\leq$ 1.6
28316	0.5162	-15.4466	0.0338115	22.69	21.28	1.241	3.385	2.467	-0.99	0.25	-111	6	$\leq$ 1.6
26856	0.4692	-15.4438	0.0344805	22.35	20.94	1.991	4.473	3.291	-0.38	0.31	-115	6	$\leq$ 1.6
27091	0.4726	-15.4410	0.0354185	22.41	21.25	1.273	3.422	2.340	-1.29	0.24	-130	6	$\leq$ 1.6
28220	0.4741	-15.4387	0.0372675	22.67	21.17	0.903	3.485	2.757	-1.18	0.25	-145	6	4.2
27342	0.5131	-15.4361	0.0424025	22.47	21.09	1.040	3.951	2.198	-1.22	0.25	-141	5	1.8
28371	0.5223	-15.4334	0.0506345	22.70	21.31	1.122	2.208	1.219	-2.05	0.17	-109	6	18.0
28056	0.5086	-15.4305	0.0469298	22.63	21.28	1.263	3.507	3.106	-0.94	0.26	-130	6	$\leq$ 1.6
27590	0.5008	-15.4281	0.0476470	22.53	21.16	1.048	3.247	2.778	-1.24	0.24	-126	7	2.9
27004	0.5074	-15.4248	0.0534145	22.39	21.22	1.518	3.831	3.092	-0.82	0.27	-107	9	$\leq$ 1.6
27856	0.5229	-15.4224	0.0627850	22.59	21.13	1.721	3.454	2.367	-1.07	0.25	-98	8	1.8
27548	0.4668	-15.4210	0.0611249	22.52	21.20	1.716	3.654	3.285	-0.71	0.28	-149	7	$\leq$ 1.6
28328	0.5189	-15.4199	0.0637268	22.69	21.06	1.682	4.416	2.915	-0.55	0.29	-156	6	$\leq$ 1.6
28682	0.4792	-15.4188	0.0599319	22.76	21.43	0.787	3.122	2.674	-1.35	0.23	-116	8	3.5
31087	0.4885	-15.4176	0.0603162	23.21	21.47	0.996	2.930	2.110	-1.42	0.21	-133	6	18.0
27765	0.4819	-15.4161	0.0628594	22.57	21.41	1.439	2.975	1.982	-1.46	0.22	-144	6	$\leq$ 1.6
28590	0.4775	-15.4118	0.0691717	22.75	21.13	1.329	3.127	2.235	-1.32	0.23	-148	6	14.0
27189	0.4786	-15.4095	0.0719565	22.44	21.26	1.509	3.021	2.529	-1.27	0.24	-130	6	$\leq$ 1.6
26226	0.5257	-15.4046	0.0845370	22.13	20.84	1.456	2.996	2.437	-1.41	0.23	-103	6	$\leq$ 1.6
28196	0.4656	-15.4022	0.0843228	22.66	21.26	0.946	3.665	2.272	-1.27	0.24	-115	6	4.2
28736	0.4630	-15.3996	0.0883728	22.77	21.25	1.082	3.432	1.590	-1.51	0.22	-137	6	18.0
28821	0.5198	-15.3966	0.0920141	22.79	21.51	1.067	3.489	1.903	-1.38	0.23	-139	8	2.4
29499	0.5074	-15.3936	0.0928048	22.92	21.41	1.078	2.906	1.921	-1.54	0.21	-118	6	18.0
27734	0.5055	-15.3913	0.0954310	22.57	21.28	1.539	2.910	1.823	-1.51	0.21	-123	7	1.8
29590	0.4825	-15.3878	0.0992865	22.94	21.49	1.346	4.305	2.224	-0.86	0.27	-130	9	2.8
27667	0.4857	-15.3850	0.1026929	22.55	21.30	0.789	3.592	2.271	-1.38	0.24	-153	6	$\leq$ 1.6
27192	0.4952	-15.3816	0.1069359	22.44	21.00	1.148	2.765	1.947	-1.68	0.21	-107	8	3.8
27515	0.5155	-15.3759	0.1168678	22.51	20.92	1.806	3.416	3.241	-0.78	0.27	-124	6	1.8
28531	0.4731	-15.3737	0.1185451	22.73	21.15	1.946	3.563	2.593	-0.84	0.26	-127	6	2.6
28064	0.5206	-15.3691	0.1266431	22.64	21.42	1.198	2.689	2.413	-1.48	0.22	-126	6	$\leq$ 1.6
19203	0.5036	-15.3643	0.1298484	24.05	21.47	0.970	2.766	1.639	-1.42	0.19	-189	7	18.0
16415	0.5188	-15.3616	0.1356525	22.59	21.21	1.645	3.217	2.266	-1.21	0.24	-117	5	2.0
16348	0.4626	-15.3572	0.1414459	22.52	21.06	1.378	4.115	2.913	-0.79	0.28	-149	6	1.8
16163	0.5051	-15.3542	0.1430462	22.30	21.10	1.103	3.501	2.765	-1.21	0.25	-146	6	$\leq$ 1.6
16218	0.5013	-15.3490	0.1494224	22.38	21.11	1.325	3.064	2.466	-1.36	0.23	-144	6	$\leq$ 1.6
16335	0.5224	-15.3465	0.1555663	22.51	21.22	0.667	2.320	0.911	-2.32	0.16	-148	6	3.2
16326	0.5105	-15.3438	0.1570543	22.50	21.12	1.017	2.970	1.857	-1.67	0.21	-111	7	3.2
16329	0.4811	-15.3393	0.1619626	22.50	21.30	1.208	2.929	2.136	-1.52	0.22	-140	6	$\leq$ 1.6
16225	0.4775	-15.3361	0.1663648	22.39	21.21	0.629	3.286	1.653	-1.79	0.21	-130	5	$\leq$ 1.6
16511	0.5299	-15.3321	0.1753224	22.69	21.23	0.760	3.408	1.502	-1.68	0.21	-148	6	8.0
16354	0.4947	-15.3299	0.1738444	22.53	21.21	0.797	3.207	1.974	-1.61	0.21	-162	6	2.6
16298	0.4728	-15.3269	0.1786507	22.46	21.09	1.175	3.025	2.082	-1.53	0.22	-144	6	2.6
16413	0.4822	-15.3213	0.1852281	22.59	21.13	1.197	3.741	2.747	-1.02	0.26	-132	7	1.8
16474	0.5200	-15.3183	0.1910044	22.65	21.11	0.867	2.697	1.853	-1.77	0.20	-130	5	16.0
16299	0.5024	-15.3144	0.1941447	22.46	21.07	0.731	3.259	2.277	-1.53	0.23	-151	5	3.2
16259	0.4855	-15.3111	0.1982649	22.43	21.04	0.937	3.042	2.702	-1.40	0.23	-151	6	2.7
16300	0.5033	-15.3084	0.2019618	22.46	21.20	1.605	2.852	2.630	-1.26	0.24	-147	9	$\leq$ 1.6

TABLE 4

Binned Age Metallicity Statistics

Variable	$t < 1$	$1 \leq t \leq 6$	$t > 6$
$\langle [Fe/H] \rangle$ (dex)	-1.21 ± 0.05	-1.23 ± 0.04	-1.55 ± 0.07
$\langle \sigma_{[Fe/H]} \rangle$ (dex)	0.42	0.34	0.22
$\langle v_{hel} \rangle$ (km s^{-1})	-129 ± 1	-130 ± 1	-136 ± 2
$\langle \sigma_v \rangle$ (km s^{-1})	17	16	22
$\langle t \rangle$ (Gyr)	0.2	3.0	15
$\langle r_{ell} \rangle$ (deg.)	0.07	0.09	0.08
$\langle \sigma_r \rangle$ (deg.)	0.05	0.06	0.05
n	30	35	13

Note. — Average values in three age bins, for various parameters of our WLM stellar sample.

TABLE 5
SUBPOPULATION $\frac{v_{rot}}{\sigma_v}$ RATIOS

Component	v_{rot}	σ_v	$\frac{v_{rot}}{\sigma_v}$
Full Sample	20.78	17.53	1.19
Metal Rich	20.61	14.29	1.44
Metal Poor	19.64	19.91	0.99
$t < 1$ Gyr	22.55	17.31	1.30
$1 \leq t \leq 6$ Gyr	17.52	16.14	1.09
$t > 6$ Gyr	9.90	15.20	0.65
HI-like velocities (”disk”)	40.50	13.50	3.00
non-HI-like velocities (”halo”)	22.86	18.67	1.23

NOTE. — The final two rows separate the sample based on those stars that fall in the same position-velocity space as the Kepley et al. (2007) HI velocity data.